

## Full length article

Role of the X and n factors in ion-irradiation induced phase transformations of  $M_{n+1}AX_n$  phases

Chenxu Wang <sup>a,b</sup>, Tengfei Yang <sup>a</sup>, Cameron L. Tracy <sup>b</sup>, Jingren Xiao <sup>a</sup>, Shaoshuai Liu <sup>a</sup>, Yuan Fang <sup>a</sup>, Zhanfeng Yan <sup>a</sup>, Wei Ge <sup>a</sup>, Jianming Xue <sup>a</sup>, Jie Zhang <sup>c</sup>, Jingyang Wang <sup>c</sup>, Qing Huang <sup>d</sup>, Rodney C. Ewing <sup>b</sup>, Yugang Wang <sup>a,\*</sup>

<sup>a</sup> State Key Laboratory of Nuclear Physics and Technology, Center for Applied Physics and Technology, Peking University, Beijing 100871, China

<sup>b</sup> Department of Geological Sciences, Stanford University, Stanford, CA 94305, USA

<sup>c</sup> Shenyang National Laboratory for Materials Science, Institute of Metal Research, Chinese Academy of Sciences, Shenyang 110016, China

<sup>d</sup> Ningbo Institute of Material Technology and Engineering, Chinese Academy of Sciences, Ningbo 315201, China

## ARTICLE INFO

## Article history:

Received 24 May 2017

Received in revised form

1 November 2017

Accepted 3 November 2017

Available online 4 November 2017

## Keywords:

MAX phases

Irradiation effects

Phase transformations

## ABSTRACT

Phase transitions induced in hcp  $M_{n+1}AX_n$  phases ( $Ti_2AlN$ ,  $Ti_2AlC$ , and  $Ti_4AlN_3$ ) by 1 MeV  $Au^+$  ion irradiation were investigated, over a series of ion fluences ranging from  $1 \times 10^{14}$  to  $2 \times 10^{16}$  ions  $cm^{-2}$ , by transmission electron microscopy (TEM) and synchrotron grazing incidence X-ray diffraction (GIXRD). Irradiation-induced structural evolutions were observed using high-resolution TEM (HRTEM) imaging and selected area electron diffraction (SAED). Based on phase contrast imaging and electron diffraction pattern (EDP) simulations, the atomic-scale mechanisms for the phase transitions were determined. Transformations of the initial hcp phases to the intermediate  $\gamma$ -phases and fcc phases were driven by the formation of Ti/Al antisite defects and extended stacking faults induced by ion irradiation. By comparing the transformation behavior of  $Ti_2AlN$  with that of  $Ti_2AlC$  and  $Ti_4AlN_3$  under the same irradiation conditions, using both the experimental data and first-principles calculations, the role of the X and n parameters in the radiation responses of  $M_{n+1}AX_n$  phases were elucidated. The susceptibilities of materials in this Ti-Al-X (X = C, N) system to irradiation-induced phase transitions were determined with respect to the bonding characteristics and compositions of these MAX phases.  $Ti_2AlC$  is slightly less susceptible to the radiation-induced phase transformation than  $Ti_2AlN$ , which is attributed to the stronger Ti-Al bond covalency in  $Ti_2AlN$ .  $Ti_4AlN_3$  is more resistant to radiation-induced phase transformations than is  $Ti_2AlN$ , due to the lower Al content and lower anion vacancy ratio in the irradiation-induced solid solution phases.

© 2017 Acta Materialia Inc. Published by Elsevier Ltd. All rights reserved.

## 1. Introduction

Ternary compounds with the formula  $M_{n+1}AX_n$  (referred to as MAX phases), where M represents an early transition metal, A is an A-group element, X is nitrogen or carbon, and  $n = 1, 2$ , or 3, exhibit nano-layered structures and possess unique combinations of properties typical of both metals and ceramics. These include easy machinability, high thermal and electrical conductivities, and excellent high-temperature resistance to oxidation and corrosion [1–8]. These remarkable properties make MAX phases promising candidate materials for future fission and fusion reactors [9],

wherein materials are likely to experience both high temperatures and severe radiation damage. For example, these materials have been proposed as coatings on zirconium alloy fuel cladding materials that are used as the first containment of nuclear fuel in Gen-II/III LWRs (light water reactors) [10]. Such innovative fuel cladding material concepts are expected to be characterized by an improved accident tolerance when compared to the commercially available zircaloy clads.

Irradiation of materials by neutrons or ions leads to the production of large numbers of defects, including point defects, extended dislocation loops and stacking faults. Extensive defect accumulation can cause order-disorder transformations and even amorphization, often degrading the physical, chemical, electrical, thermal and mechanical properties of materials. Therefore, the

\* Corresponding author.

E-mail address: [ygwang@pku.edu.cn](mailto:ygwang@pku.edu.cn) (Y. Wang).

microstructural response of MAX phases to irradiation plays an important role in their application in nuclear systems. Previously, alpha particle irradiation-induced He bubble formation [11,12] and ion irradiation-induced phase modification [13–16] in MAX phases have been studied. Liu et al. [13] observed an ion irradiation-induced transformation in  $Ti_3Si_{0.90}Al_{0.10}C_2$  at relatively low ion fluences. More recently, the structural evolution of  $Ti_2AlC$  irradiated with  $Au^+$  ions to a relatively high fluence was investigated, revealing a phase transition from the initial hcp structure to an fcc structure [15]. However, few studies have addressed the detailed processes of irradiation-induced phase transitions in N-based MAX phases.

There are four compositional factors that describe  $M_{n+1}AX_n$  phases: M, A, X, and n, which determine the physical and mechanical properties of these materials. Previous studies have shown clear compositional variation in, for example, elastic properties [17], transport properties [18], optical conductivity [19] and oxidation properties [20]. It has been shown experimentally [21–23] that the phase transitions and amorphization induced by ion irradiation of MAX phases depend strongly on composition. Recently, we investigated the amorphization resistance of  $Cr_2AlC$  and  $V_2AlC$ , possessing different M cations, under ion irradiation, showing that  $Cr_2AlC$  is extremely sensitive to irradiation and eventually becomes completely amorphous, while  $V_2AlC$  remains crystalline [21]. Whittle et al. [22] characterized  $Ti_3AlC_2$  and  $Ti_3SiC_2$ , two representative MAX phases in which only the A elements differ, revealing different radiation tolerances between them. First-principle calculations support these findings [24,25]. Zhao et al. [24] argues that differences in bonding between  $Ti_3AlC_2$  and  $Ti_3SiC_2$  lead to the different radiation tolerance of these two materials. However, the role of the X and n factors in the radiation tolerance or amorphization resistance of the  $M_{n+1}AX_n$  compounds is still unknown.

Here, we report the phase transitions of  $Ti_2AlN$ ,  $Ti_2AlC$ , and  $Ti_4AlN_3$ , three typical MAX phases, under 1 MeV  $Au^+$  ion irradiation over a wide fluence range. The atomic-scale processes associated with these transformations are elucidated by complementary synchrotron grazing incidence X-ray diffraction (GIXRD) analysis and transmission electron microscopy (TEM) observations, combined with electron diffraction pattern (EDP) and phase contrast simulations. We compare  $Ti_2AlN$  with  $Ti_2AlC$  and  $Ti_4AlN_3$  under the same irradiation conditions in order to investigate the role of X and n factors in the susceptibility of MAX phases to irradiation-induced phase transitions. Based on first-principles calculations of the bonding in two of these MAX phases ( $Ti_2AlN$  and  $Ti_2AlC$ ), the degree of bond covalency is proposed as a primary determinant of radiation tolerance. Differences in the Ti/Al cation site occupancy and anion vacancy concentrations in  $Ti_2AlN$  and  $Ti_4AlN_3$  are considered as the main reasons for the different structural responses of these two N-based MAX phases. These proposed criteria for radiation response can be further applied to develop MAX phases and related materials with superior performance and resilience in nuclear energy applications.

## 2. Experimental and theoretical methods

Dense polycrystalline samples of  $Ti_2AlN$ ,  $Ti_2AlC$ , and  $Ti_4AlN_3$  were synthesized by reactive hot isostatic pressing (HIP) at the Shenyang National Laboratory for Materials Science and Ningbo Institute of Materials Technology and Engineering (NIMTE). For example, for the synthesis of  $Ti_2AlN$ , stoichiometric ratios of Ti, Al, and TiN powders (molar ratio 1:1:1) were mixed and ball-milled for 10 h. Stoichiometrically appropriate ratios of precursor powders were similarly mixed and milled for the other two compounds. The powders were cold-pressed under a pressure of 5 MPa in a graphite

mold, then hot-pressed under a pressure of 25 MPa at 1400 °C in a flowing argon atmosphere for 1 h. Finally, the samples were cooled to ambient conditions. Further details of the synthesis of these samples can be found elsewhere [26–28]. The grain sizes of all three compounds were between several micrometers and several tens of micrometers. The resulting dense pellets were polished with diamond paste suspensions then washed with acetone.

The samples were irradiated using the tandem 1.7 MV ion accelerator at Peking University. All samples were simultaneously exposed at room temperature to a beam of 1 MeV  $Au^+$  ions, which can induce more displacement per atom (dpa) at the same ion influences. The beam direction was perpendicular to the sample surfaces. The ion beam current was maintained below 1  $\mu A\text{ cm}^{-2}$  to avoid significant bulk heating of the samples. The irradiation was performed over a series of ion fluences ranging from  $1 \times 10^{14}$  to  $2 \times 10^{16}$  ions  $\text{cm}^{-2}$ . The corresponding irradiation-induced damage ranges from around 0.7 dpa to over 150 dpa. The penetration of  $Au^+$  ions into the samples and the damage distribution were calculated using SRIM code, as shown in Fig. 1. The assumed threshold displacement energies were: 25 eV for Ti and Al, and 28 eV for C and N [29].

Irradiation-induced modifications to the long-range atomic structures of these materials were characterized by GIXRD, performed at the 1W1A beamline station of the Beijing Synchrotron Radiation Facility (BSRF) with an X-ray beam of wavelength  $\lambda = 0.1547$  nm. The incident angle and the  $2\theta$  step interval of the X-ray beam were set to 0.5° and 0.05°, respectively, such that the probed sample depth in the GIXRD measurements was ~200 nm, excluding significant signal from the unirradiated substrate in the collected diffraction patterns. The process of the phase transitions after irradiation was determined through high resolution imaging and selected area electron diffraction (SAED) using a 200 keV Tecnai F20 TEM at the Electron Microscopy Laboratory of Peking University. TEM cross-sectional thin foils were prepared by mechanical polishing of the irradiated samples down to ~20  $\mu\text{m}$ , followed by ion milling to obtain a wedge for sufficient electron transparency. EDPs and phase contrast images were simulated using CrystalMaker software and NCEMSS [30], respectively.

First-principle calculations were performed within the Vienna *ab initio* Simulation Package (VASP) [31,32]. Projector augmented-wave (PAW) potentials [33], together with the widely used electronic exchange-correlation function of the generalized gradient approximation (GGA) [34] in Perdew-Burke-Ernzerhof (PBE) [35], were employed. All configurations were studied on a mesh of  $10 \times 10 \times 2$  irreducible  $k$ -points within the generation scheme of Monkhorst-Pack [36]. All defect calculations were performed within a  $2 \times 2 \times 3$  supercell containing 96 atoms (12 conventional unit cells with 8 atoms in each unit cell) for  $Ti_2AlX$  (X = C, N). The total energy was converged to better than 0.1 meV for a plane wave cutoff of 500 eV. During defect calculations, the lattice vectors of the cells and all the atoms were allowed to relax until atomic forces were less than 0.01 eV/ $\text{\AA}$ .

## 3. Results

As a typical 211-type N-based MAX phase,  $Ti_2AlN$  shares an isomorphous hexagonal-close-packed structure (space group  $P6_3/mmc$ ) with  $Ti_2AlC$ , differing only in unit cell parameter and slightly in the specific position of the Ti atoms, as shown in Table 1. For the 211-type MAX phases, the atomic structure consists of two layers of edge-sharing  $Ti_6X$  (X = C, N) octahedra interleaved by close-packed Al layers, with four M atoms in 4f Wyckoff positions, two Al atoms in 2d positions, and two C atoms in 2a positions, as shown in Fig. 2(a–c). The cation layer stacking sequence of Ti and Al atoms in  $Ti_2AlX$  (X = C, N) along [0001] is represented by ABABAB, where the

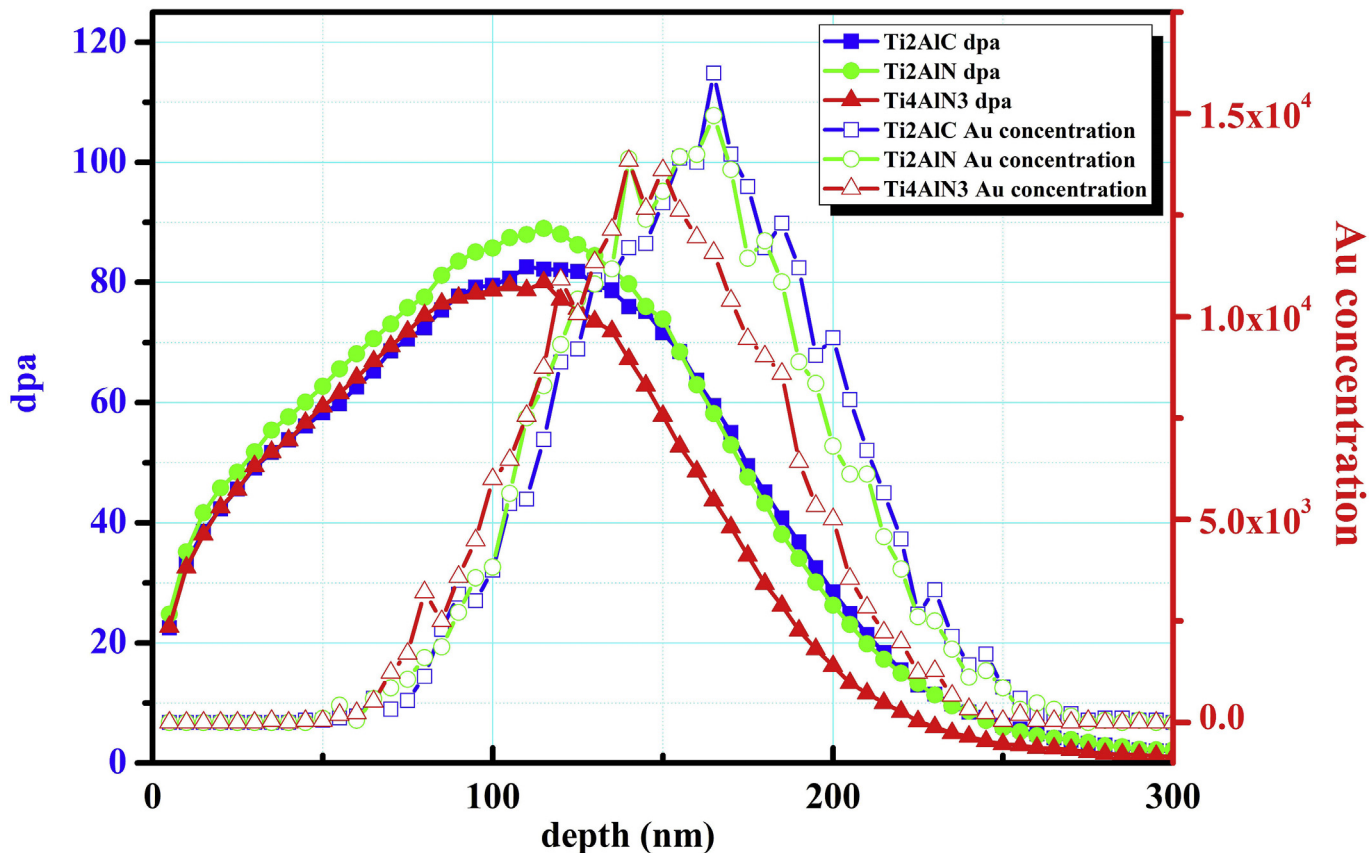


**Fig. 1.** Depth profiles of damage level, expressed in displacements per atom (dpa), and implanted ion concentration induced by 1 MeV Au $^{+}$  ion irradiation at  $1 \times 10^{16} \text{ cm}^{-2}$  in Ti<sub>2</sub>AlN, Ti<sub>2</sub>AlC and Ti<sub>4</sub>AlN<sub>3</sub>. Data were calculated using the SRIM code.

**Table 1**  
Structural parameters of Ti<sub>2</sub>AlX (X = C, N) and Ti<sub>4</sub>AlN<sub>3</sub>.

Formula	Ti <sub>2</sub> AlC [60]	Ti <sub>2</sub> AlN [61]	Ti <sub>4</sub> AlN <sub>3</sub> [62]
space group	$P\bar{6}_3/mmc(194)$	$P\bar{6}_3/mmc(194)$	$P\bar{6}_3/mmc(194)$
unit cell parameters (nm)	$a = 0.306$ $c = 1.360$	$a = 0.299$ $c = 1.361$	$a = 0.299$ $c = 2.339$
density (g/cm $^{-3}$ )	4.11	4.27	4.58
microstructural information	Wyckoff Notation	Atomic Positions	Wyckoff Notation
	Ti (4f)	(1/3, 2/3, 0.064)	Ti (4f)
	Al (2d)	(1/3, 2/3, 3/4)	Al (2d)
	C (2a)	(0, 0, 0)	N (2a)
/	/	/	(0, 0, 0)
/	/	/	N1 (2a)
			(2/3, 1/3, 0.105)
			N2 (4f)

underlined letters refer to the Al atoms and the remainder are the Ti atoms. The C or N anions are not shown in this sequence, but occupy the octahedral interstitial sites between the close-packed Ti layers. HRTEM images and the corresponding SAED patterns obtained from the pristine Ti<sub>2</sub>AlN phase along [1120] and [1100] are shown in Fig. 2(d–g). The main structural difference between Ti<sub>2</sub>AlN and Ti<sub>4</sub>AlN<sub>3</sub> is the number of the Ti layers, arranged in Ti<sub>6</sub>N octahedra, stacked between the Al planes. For Ti<sub>4</sub>AlN<sub>3</sub>, the stacking sequence of all atoms is A $\gamma$ B $\bar{\alpha}$ B $\gamma$ A $\beta$ C $\alpha$ B $\bar{\beta}$ C $\alpha$ C along [0001] [37], where the Greek letters refer to the N positions, the underlined letters to Al layers, and the remaining letters to Ti layers, as shown in Fig. 2(h–j). The atomic configurations and the SAED patterns along [1120] and [1100] are given in Fig. 2(k–n).

### 3.1. X-ray diffraction: phase transition processes

The GIXRD patterns of Ti<sub>2</sub>AlX (X = C, N) and Ti<sub>4</sub>AlN<sub>3</sub> samples before and after irradiation to various ion fluences are shown in Fig. 3. Patterns of the original samples correspond to well-crystallized Ti<sub>2</sub>AlX (X = C, N) phases of high purity, while there is a small amount of inevitable TiN impurities (~5 wt%) in Ti<sub>4</sub>AlN<sub>3</sub> samples, as indicated by the solid triangle in Fig. 3(c). After irradiation, these three MAX phases exhibit different phase transition processes and different susceptibilities to irradiation-induced structural modification. There are three main changes observed from the diffraction patterns: attenuation of the initial diffraction peaks, broadening of the initial diffraction peaks, and the formation

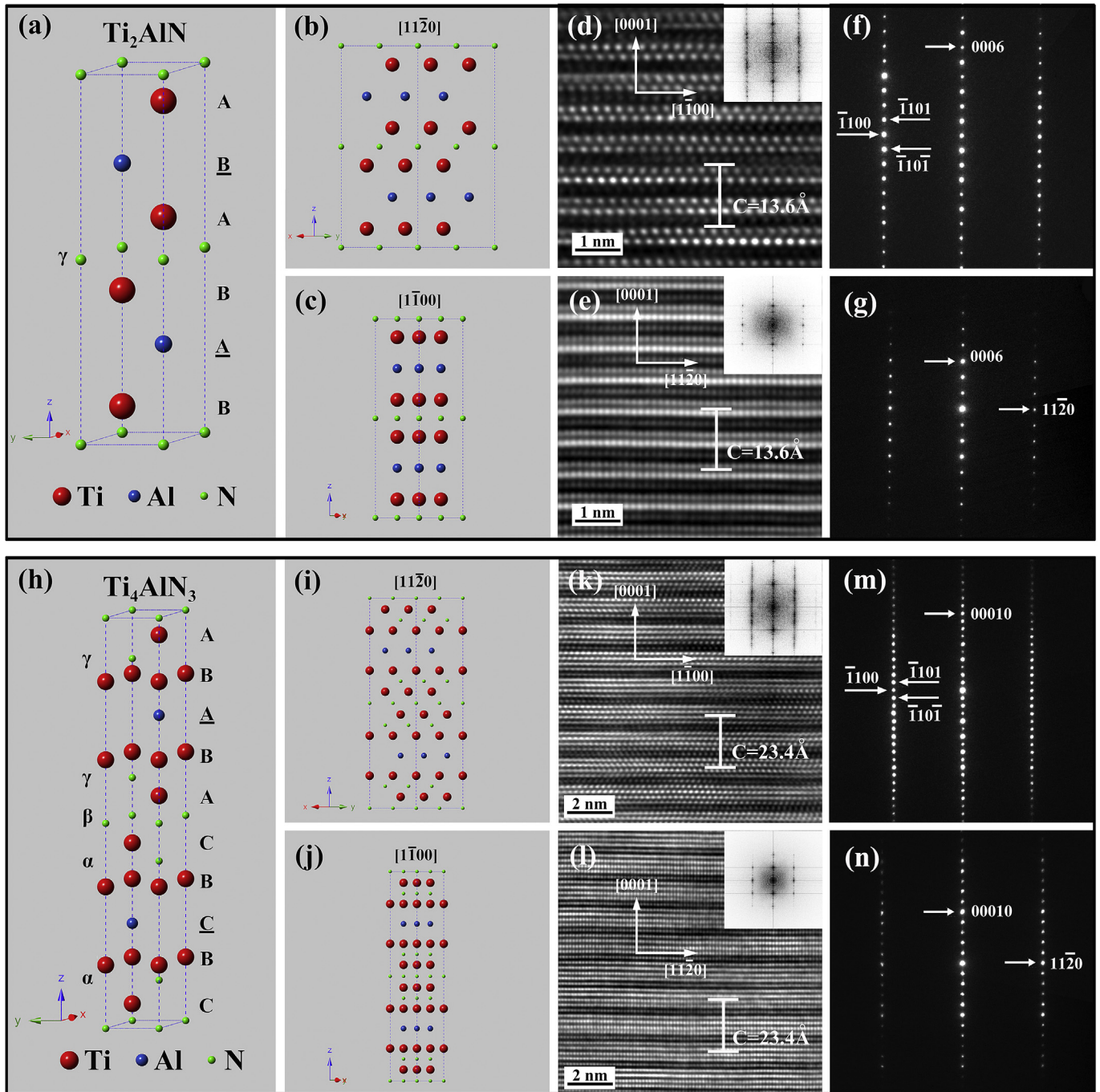


**Fig. 2.** Crystal structures with the atomic configurations in the unit cell, as well as the HRTEM images and the corresponding SAED patterns of (a–g)  $Ti_2AlN$  and (h–n)  $Ti_4AlN_3$ . The electron beam is parallel to  $[1\bar{1}\bar{2}0]$  and  $[\bar{1}\bar{1}00]$  in the top and bottom HRTEM images, respectively. The Ti and Al cation atomic sequence in  $Ti_2AlX$  ( $X = C, N$ ) along  $[0001]$  is represented by ABABAB, where the Al atoms are indicated by the underlined letters. The Greek letters indicate the anions.

of several new diffraction peaks. These changes agree with those observed in previous XRD studies of the structural evolution of irradiated  $Ti_3AC_2$  ( $A = Al, Si$ ) [11,14,38].

At the lowest fluence of  $1 \times 10^{14} \text{ cm}^{-2}$ , the intensities of all diffraction peaks corresponding to the initial hcp structure of Ti<sub>2</sub>AlN decrease significantly, with only some peaks remaining detectable, such as the (103) and (106) peaks. This indicates that ion irradiation causes the loss of ordering characteristic of the initial hcp structure. Meanwhile, continuous peak broadening can be observed with increasing ion fluence, suggesting the accumulation

of microstrain around the irradiation-induced defects. In addition, two new Bragg peaks appear in the pattern of Ti<sub>2</sub>AlN, centered at  $2\theta = 38.30^\circ$  and  $53.05^\circ$ , respectively, which indicates the formation of a new phase, designated  $\gamma$ -Ti<sub>2</sub>AlN. The measured XRD data indicate that this phase is isostructural with the phase that forms upon irradiation of Cr<sub>2</sub>AlC [21]. Using this structural interpretation, these peaks can be identified as (002) and (102) peaks, respectively, of the  $\gamma$ -Ti<sub>2</sub>AlN phase, which has the similar variation of XRD profile with that of Cr<sub>2</sub>AlC under irradiation [21] (discussed in Section 4.2). The most intense peak of the proposed  $\gamma$ -Ti<sub>2</sub>AlN phase, the (101)

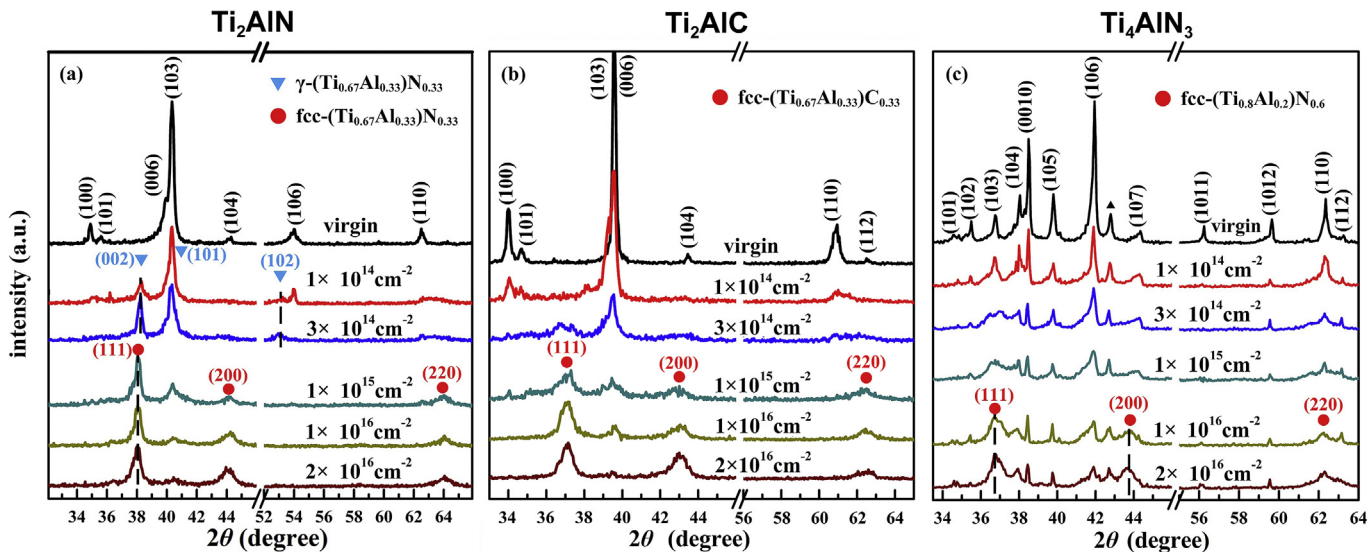


**Fig. 3.** Representative GIXRD patterns from the original and irradiated  $\text{Ti}_2\text{AlN}$  (a),  $\text{Ti}_2\text{AlC}$  (b) and  $\text{Ti}_4\text{AlN}_3$  (c) at fluences ranging from  $1 \times 10^{14} \text{ cm}^{-2}$  to  $2 \times 10^{16} \text{ cm}^{-2}$ . With increasing fluence, the diffraction maxima corresponding to all the initial phases decrease in intensity and the spectra indicate the transformation from hcp structures to fcc structures. The blue triangles and the red circles represent the peaks corresponding to the intermediate  $\gamma$ - $\text{Ti}_2\text{AlN}$  phase and the fcc phases, respectively. (For interpretation of the references to colour in this figure legend, the reader is referred to the web version of this article.)

peak, is located at  $40.30^\circ$ , such that it is indistinguishable from the original hcp (103) peak located at  $40.35^\circ$ .

As a fluence increases to  $3 \times 10^{14} \text{ cm}^{-2}$ , continuous attenuation of the original hcp peaks is observed, with the disappearance of the (100), (101), (104), and (106) peaks, while the intensities of the (002) and (102) peaks of the  $\gamma$ - $\text{Ti}_2\text{AlN}$  phase increase. This indicates the further phase transition from the original hcp  $\text{Ti}_2\text{AlN}$  phase to  $\gamma$ - $\text{Ti}_2\text{AlN}$  phase. Additionally, at a fluence of  $3 \times 10^{14} \text{ cm}^{-2}$ , all peaks shift to slightly lower  $2\theta$  angles, revealing that the unit cell expands along the  $c$  axis.

At the fluence of  $1 \times 10^{15} \text{ cm}^{-2}$ , the (101) peak from the  $\gamma$ - $\text{Ti}_2\text{AlN}$  phase becomes weak, while the (002) and (102) peaks disappear. Meanwhile, there emerge three peaks located at  $38.05^\circ$ ,  $44.10^\circ$ , and  $64.05^\circ$  which can be indexed as the (111), (200), and (220) peaks of a newly formed fcc structure. At the highest fluences of  $1 \times 10^{16} \text{ cm}^{-2}$  and  $2 \times 10^{16} \text{ cm}^{-2}$ , a continuous decrease of the remaining, low intensity of the hcp (103) peak is observed, indicating that the structure gradually transforms into the fcc structure with increasing fluence.

For  $\text{Ti}_2\text{AlC}$  compounds, similar broadening and attenuation of the characteristic peaks of the initial hcp phase is observed at relatively low ion fluences. At  $1 \times 10^{15} \text{ cm}^{-2}$ , there emerge three new peaks, i.e. (111), (200), (220) peaks, again indicating a phase transition from the original hcp structure to fcc- $\text{Ti}_2\text{AlC}$ . As the fluence increases to  $2 \times 10^{16} \text{ cm}^{-2}$ , the signal of the original hcp structure disappears, revealing that almost all the  $\text{Ti}_2\text{AlC}$  has transformed to the fcc phase.

$\text{Ti}_4\text{AlN}_3$  shows a similar transformation from the initial phase to an fcc phase. However, in contrast to the other compounds studied, the phase transition to the fcc structure begins at a relatively high ion fluence of  $1 \times 10^{16} \text{ cm}^{-2}$ . Even at the highest fluence of  $2 \times 10^{16} \text{ cm}^{-2}$ , part of the hcp structure still remains.

### 3.2. Transmission electron microscopy: atomic scale characterization

The XRD results demonstrate irradiation-induced transitions of  $\text{Ti}_2\text{AlX}$  ( $X = \text{C}, \text{N}$ ) and  $\text{Ti}_4\text{AlN}_3$ . In order to investigate the nature of these transformations at the atomic scale, TEM analysis was

performed to provide complementary crystallographic information. Fig. 4 shows the SAED patterns of  $\text{Ti}_2\text{AlX}$  ( $X = \text{C}, \text{N}$ ) and  $\text{Ti}_4\text{AlN}_3$  along [1120] after irradiation to various fluences. These patterns are consistent with the fast Fourier transforms (FFTs) of HRTEM images obtained from samples at the corresponding irradiation conditions, as shown in Fig. 5.

In  $\text{Ti}_2\text{AlN}$  irradiated at the lowest fluence of  $1 \times 10^{14} \text{ cm}^{-2}$ , the intensity of  $(000l)$  ( $l \neq 3n$ ) diffraction spots in the  $\{000l\}$  diffraction maxima and  $(\bar{1}10l)$  ( $l \neq 3n$ ) in the  $\{\bar{1}10l\}$  diffraction maxima significantly decrease, relative to patterns from the unirradiated samples. This is caused by lattice distortion due to radiation-induced damage. In the corresponding HRTEM image, shown in Fig. 5(a), the original cation periodicity of ABABAB does not change. However, the contrast in the HRTEM image of the pristine sample, with two bright layers interleaved by one dark layer (see Fig. 2(d)), has disappeared, indicating a partial transformation to the intermediate  $\gamma$ - $\text{Ti}_2\text{AlN}$  phase with an hcp structure, due to the formation of some point defects and the rearrangement of the N atoms.

As the fluence increases to  $1 \times 10^{15} \text{ cm}^{-2}$ , only the  $(000l)$  ( $l = 3n$ ) and  $(\bar{1}10l)$  ( $l = 3n$ ) diffraction spots of the initial hcp phase can be observed, as shown in Fig. 4(b). Meanwhile, there emerge two new sets of diffraction spots in the pattern, indicated by green arrows, which can be indexed as  $(\bar{1}\bar{1}1)$  and  $(002)$  diffraction spots of typical twinned fcc sequences with a rocksalt-type structure ( $Fm\bar{3}m$ ). This agrees with the XRD results, indicating that the formation of the hcp  $\gamma$ - $\text{Ti}_2\text{AlN}$  phase is followed by a transformation to the fcc structure. It should be noted that the  $(\bar{1}10l)$  ( $l = 3n$ ) diffraction spots of the hcp structure and the  $(\bar{1}\bar{1}1)$  and  $(002)$  diffraction spots of the fcc structure tend to perpendicularly coalesce with the adjacent spots, which can be explained by the increasing number of stacking faults in the basal planes. The irradiation-induced stacking faults and the formation of the fcc structure with the stacking sequences of ABCABC (or/and CBACBA) are also observed in the corresponding HRTEM image, as shown in Fig. 5(b). The transformed fcc structure possesses a specific crystallographic relationship with the original hcp structure: [1120] hcp // [110] fcc, and  $(0001)$  hcp // (111) fcc as the closed-packed plane, respectively.

With the increase of the fluence to  $1 \times 10^{16} \text{ cm}^{-2}$ , the diffraction

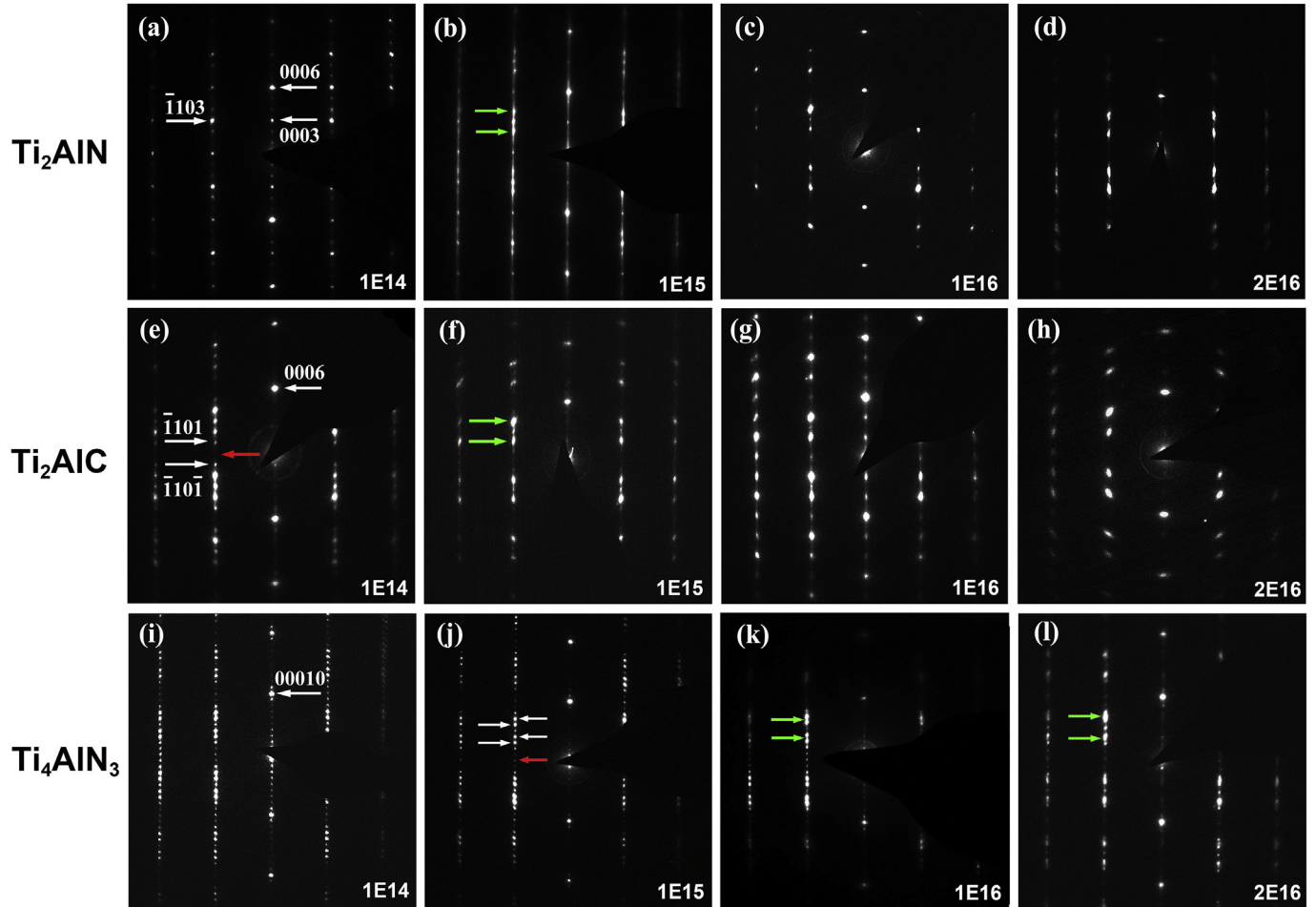


**Fig. 4.** SAED patterns of Ti<sub>2</sub>AlN (a–d), Ti<sub>2</sub>AlC (e–h) and Ti<sub>4</sub>AlN<sub>3</sub> (i–l) irradiated with 1 MeV Au<sup>+</sup> ions at  $1 \times 10^{14} \text{ cm}^{-2}$  (a, e, and i),  $1 \times 10^{15} \text{ cm}^{-2}$  (b, f, and j),  $1 \times 10^{16} \text{ cm}^{-2}$  (c, g, and k), and  $2 \times 10^{16} \text{ cm}^{-2}$  (d, h, and l). In all cases, the electron beam is parallel to [1120]. The green arrows indicate the diffraction spots of new fcc structures. The red arrows indicate the significant attenuation of the  $(\bar{1}100)$  diffraction spot. (For interpretation of the references to colour in this figure legend, the reader is referred to the web version of this article.)

spots of the original hcp structure and the hcp  $\gamma$ -phase structure significantly attenuate. They fully disappear at the highest fluence of  $2 \times 10^{16} \text{ cm}^{-2}$ , demonstrating a nearly complete transformation to the fcc phase. This result is confirmed by the HRTEM image, shown in Fig. 5(c), in which only the nano-sized twinned fcc structure can be observed. The structures of Ti<sub>2</sub>AlN under irradiation at different fluences are described in Table 2.

A similar transformation process from the initial hcp structure to an fcc structure was observed in Ti<sub>2</sub>AlC. At a fluence of  $1 \times 10^{14} \text{ cm}^{-2}$ , the  $(000l)$  ( $l \neq 6n$ ) diffraction spots in the  $\{000l\}$  diffraction maxima and the  $(\bar{1}10l)$  ( $l \neq 6n, 6n \pm 1$ ) spots in the  $\{\bar{1}10l\}$  diffraction maxima attenuate, as compared with the original pattern of 211-type MAX phases, which indicates the transformation of the initial hcp structure to the hcp  $\gamma$ -Ti<sub>2</sub>AlC phase. This is confirmed by the variation of the stacking sequence in the corresponding HRTEM image [15], as shown in Fig. 5(d). As the fluence increases to  $1 \times 10^{15} \text{ cm}^{-2}$ , diffraction spots corresponding to the fcc structure appear, and gradually increase in intensity with increasing fluence. In addition, at a fluence of  $1 \times 10^{16} \text{ cm}^{-2}$ , there appear some spots which belong to neither the original hcp structure nor the fcc structure, whereas Ti<sub>2</sub>AlN has already completely transformed to the fcc-Ti<sub>2</sub>AlN structure. The presence of this additional phase, designated the  $\delta$ -Ti<sub>2</sub>AlC phase (space group  $P\bar{3} m1$ ,  $a = 0.302 \text{ nm}$ ,  $c = 0.727 \text{ nm}$  [15]), is confirmed by the corresponding HRTEM image, which exhibits a threefold modulated

structure with two lighter layers interleaved by one darker layer, as shown in Fig. 5(f). At the highest fluence of  $2 \times 10^{16} \text{ cm}^{-2}$ , the diffraction spots of the hcp structure fully disappear, confirming a complete phase transformation to the fcc structure. This result indicates that Ti<sub>2</sub>AlC is slightly more resistant to the radiation-induced phase transformation than Ti<sub>2</sub>AlN.

In contrast to the compounds discussed above, the threshold fluence for the onset of the transformation to the fcc phase in Ti<sub>4</sub>AlN<sub>3</sub> is  $1 \times 10^{16} \text{ cm}^{-2}$ , at which the characteristic diffraction spots of the fcc structure can be observed, as shown in Fig. 4(k). However, since the structural transformation from the initial hcp phase to the fcc phase is not complete, two sets of diffraction spots are apparent. Even at the highest fluence of  $2 \times 10^{16} \text{ cm}^{-2}$ , there still exists a considerable amount of the hcp structure, as shown in Fig. 4(l), indicating that Ti<sub>4</sub>AlN<sub>3</sub> is highly resistant to the radiation-induced structural phase transition, relative to Ti<sub>2</sub>AlX (X = C, N), as shown in Table 2.

In order to further verify the structural evolution, TEM images of the three compounds along [1100] are shown in Figs. 6 and 7. As the fluence increases, the  $(000l)$  ( $l \neq 6n$ ) and  $(11\bar{2}l)$  ( $l \neq 6n$ ) diffraction spots in Ti<sub>2</sub>AlN and Ti<sub>2</sub>AlC, as well as the  $(000l)$  ( $l \neq 10n$ ) and  $(11\bar{2}l)$  ( $l \neq 10n$ ) diffraction spots in Ti<sub>4</sub>AlN<sub>3</sub> along [1100] gradually attenuate, relative to those in the patterns of the pristine compounds. This results from the loss of the long-range order induced by irradiation. Once the fluence reaches  $1 \times 10^{15} \text{ cm}^{-2}$ , these

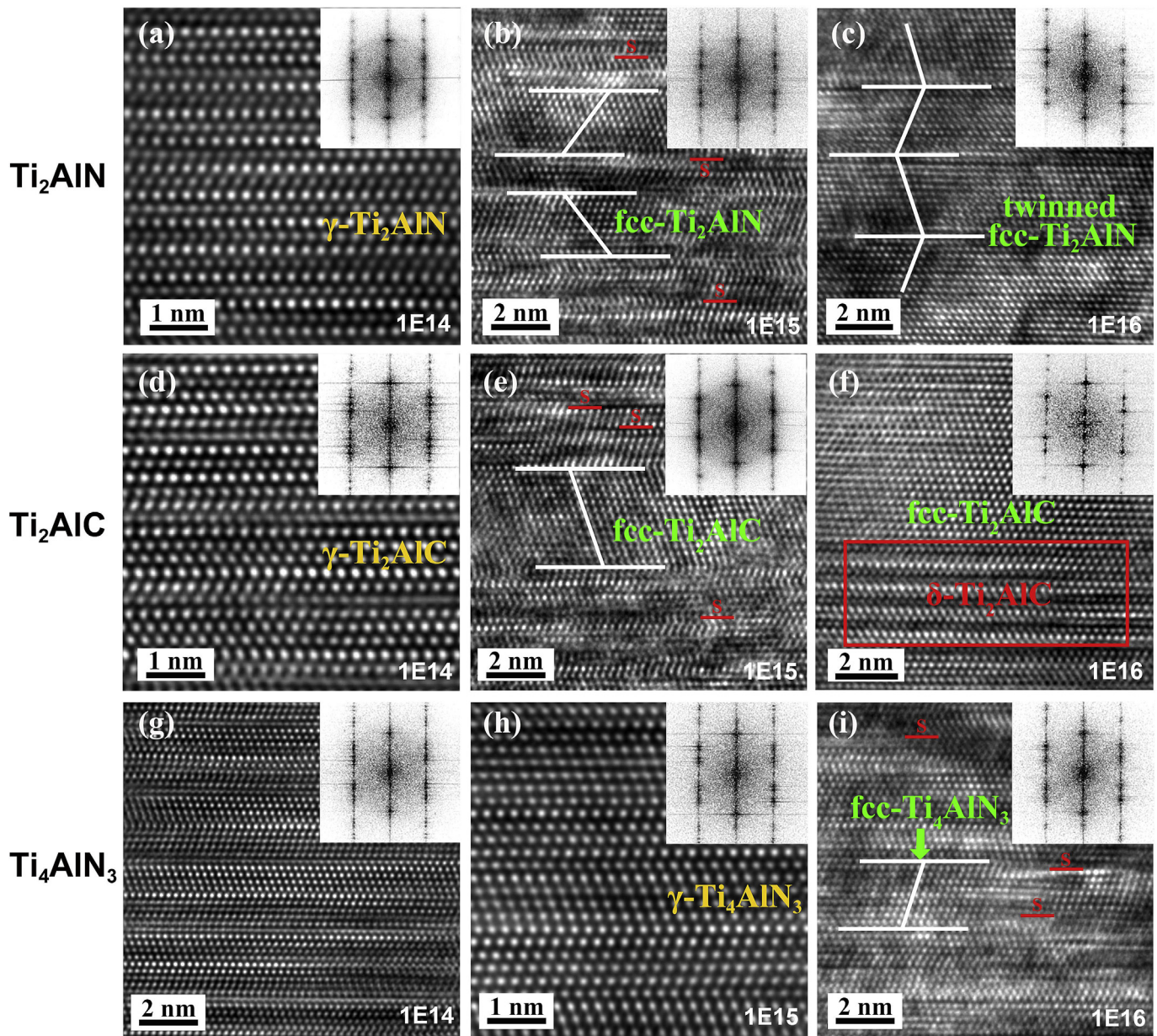


**Fig. 5.** HRTEM images of  $\text{Ti}_2\text{AlN}$  (a–c),  $\text{Ti}_2\text{AlC}$  (d–f) and  $\text{Ti}_4\text{AlN}_3$  (g–i) irradiated with  $1 \text{ MeV Au}^+$  ions at  $1 \times 10^{14} \text{ cm}^{-2}$  (a, d, and g),  $1 \times 10^{15} \text{ cm}^{-2}$  (b, e, and h),  $1 \times 10^{16} \text{ cm}^{-2}$  (c, f, and i). The electron beam is parallel to  $[1\bar{1}\bar{2}0]$  and the FFTs are given in the insets. The transformed fcc phases and the stacking faults are indicated between the white lines and by the red lines, respectively. (For interpretation of the references to colour in this figure legend, the reader is referred to the web version of this article.)

**Table 2**  
Structures of  $\text{Ti}_2\text{AlX}$  ( $X = \text{C}, \text{N}$ ) and  $\text{Ti}_4\text{AlN}_3$  at different fluences.

Fluence ( $\text{cm}^{-2}$ )	$1 \times 10^{14}$ – $3 \times 10^{14}$	$1 \times 10^{15}$	$1 \times 10^{16}$	$2 \times 10^{16}$
$\text{Ti}_2\text{AlN}$	$\gamma$	$\gamma + \text{fcc}$	almost fcc	fcc
$\text{Ti}_2\text{AlC}$	$\gamma$	$\gamma + \text{fcc}$	$\delta + \text{fcc}$	fcc
$\text{Ti}_4\text{AlN}_3$	hcp	$\gamma$	$\gamma + \text{fcc}$	$\gamma + \text{fcc}$

diffraction spots in  $\text{Ti}_4\text{AlN}_3$  remain visible, while those in  $\text{Ti}_2\text{AlN}$  and  $\text{Ti}_2\text{AlC}$  completely disappear, further indicating the lesser radiation tolerance of the hcp phases of the latter two compositions. In the corresponding HRTEM images in Fig. 7, the phase contrast corresponding to the initial nanolayered structure of  $\text{Ti}_2\text{AlN}$  (a) and  $\text{Ti}_2\text{AlC}$  (b) is no longer visible at this fluence, and the interlayer distances along  $[0001]$  become homogeneous, which is consistent

with the observations along  $[11\bar{2}0]$ . In contrast, the nanolayered phase contrast in  $\text{Ti}_4\text{AlN}_3$  can still be observed by  $1 \times 10^{15} \text{ cm}^{-2}$ , as shown in Fig. 7(c). Although the primary ABABAB periodicity of the hcp phase and the ABCABC periodicity of the irradiation-induced fcc structure cannot be distinguished along  $[1\bar{1}00]$ , the accuracy of the structural analysis can be enhanced by considering the SAED patterns from two different orientations.

## 4. Discussion

### 4.1. Mechanism of the hcp- $\gamma$ -fcc phase transition

As shown by the XRD and TEM results, a series of phase transitions occur after irradiation in all three materials studied. In order to investigate the detailed processes and mechanism of these

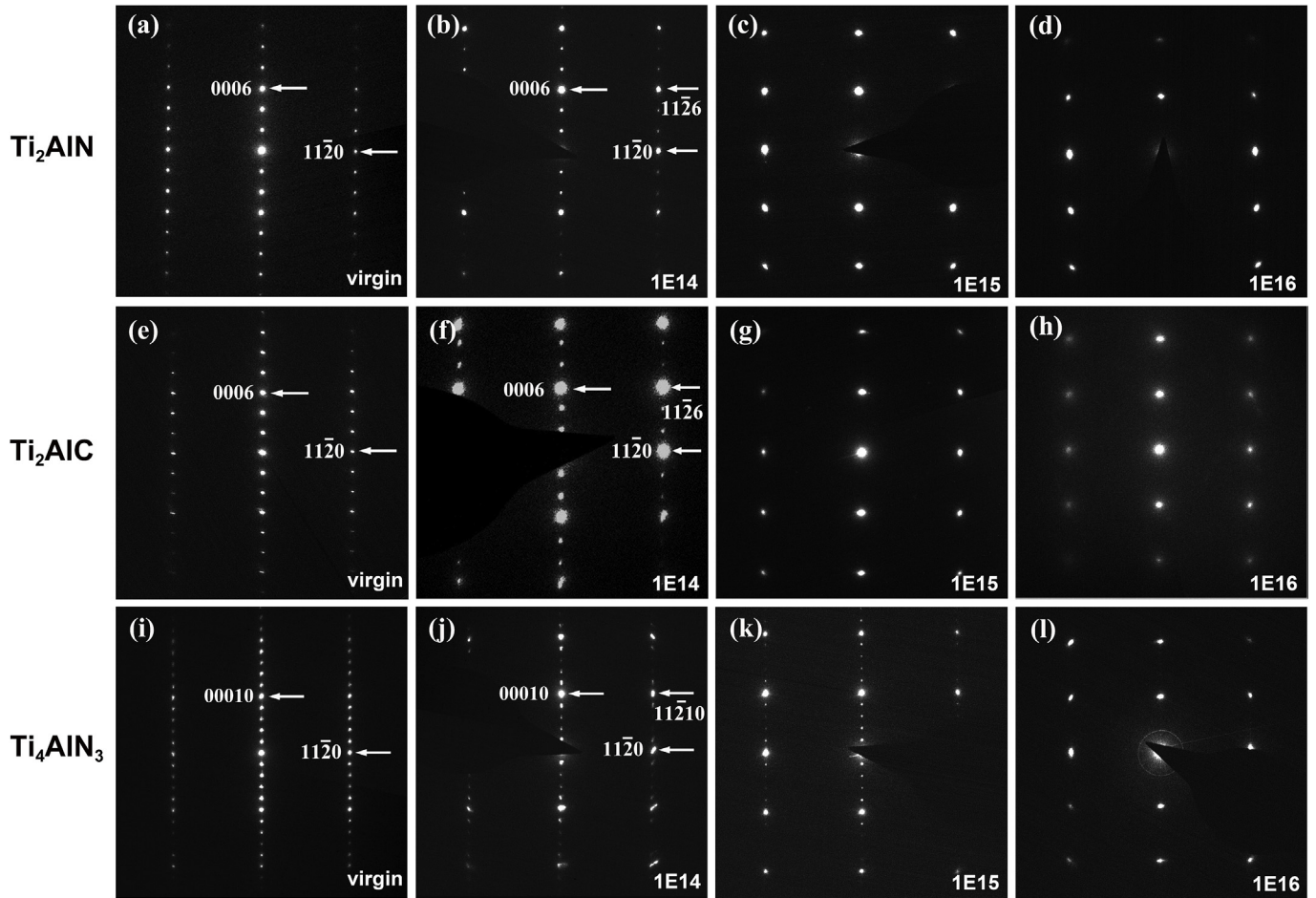


**Fig. 6.** SAED patterns of Ti<sub>2</sub>AlN (a–c), Ti<sub>2</sub>AlC (d–f) and Ti<sub>4</sub>AlN<sub>3</sub> (g–i) before (a, e, and i) and after irradiated with 1 MeV Au<sup>+</sup> ions at  $1 \times 10^{14} \text{ cm}^{-2}$  (b, f and j),  $1 \times 10^{15} \text{ cm}^{-2}$  (c, g and k), and  $1 \times 10^{16} \text{ cm}^{-2}$  (d, h and l). The electron beam is parallel to [1̄100].

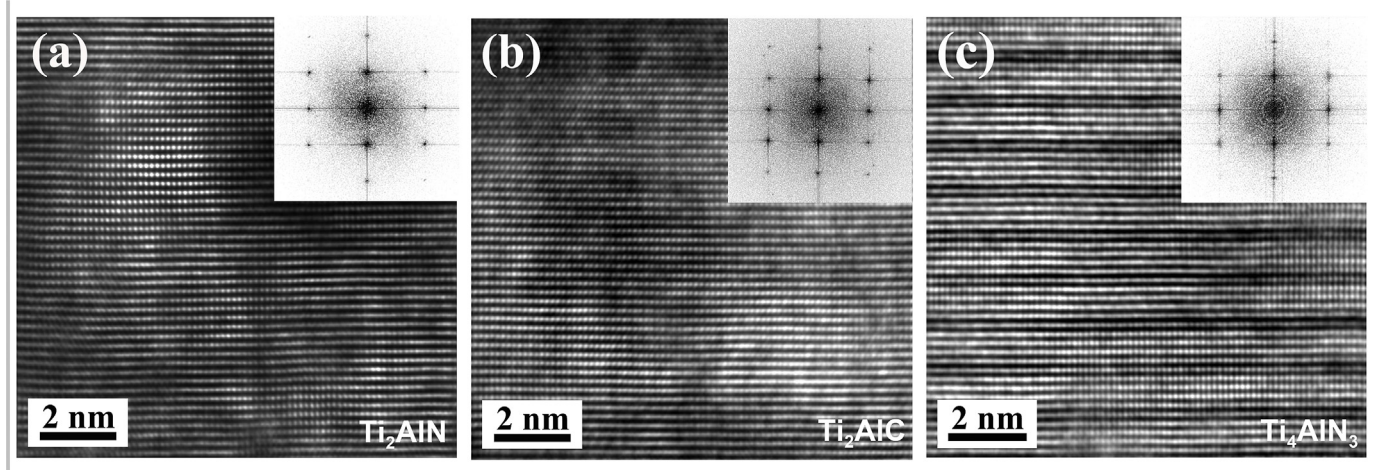


**Fig. 7.** HRTEM images of Ti<sub>2</sub>AlN (a), Ti<sub>2</sub>AlC (b) and Ti<sub>4</sub>AlN<sub>3</sub> (c) irradiated with 1 MeV Au<sup>+</sup> ions to a fluence of  $1 \times 10^{15} \text{ cm}^{-2}$ . The electron beam is parallel to [1̄100] and FFTs are given in the insets.

transitions, EDP and phase contrast simulations were performed. For simplicity, this analysis focuses on Ti<sub>2</sub>AlN, as similar transitions occur in all three compounds, such that this analysis is applicable to the MAX phases generally. In the fluence range from  $1 \times 10^{14}$  to  $3 \times 10^{14} \text{ cm}^{-2}$ , the appearance of new peaks in the XRD patterns

(see Fig. 3) and the attenuation of some diffraction spots in the SAED patterns (see Fig. 4) suggest a phase transition from the original hcp structure to a  $\gamma$ -Ti<sub>2</sub>AlN phase with the same ABAB stacking sequence, which is demonstrated in the HRTEM image in Fig. 5.

In previous studies of MAX phases using the *ab initio* simulations [24,39], the formation energies of all defects were calculated, including interstitials, Frenkel pair defects and antisite defects. The results showed that the formation energies of antisite defects,  $\text{Al}_{\text{Ti}(2)}$  (0.74 eV) in  $\text{Ti}_3\text{AlC}_2$  and  $\text{Si}_{\text{Ti}(2)}$  (2.13 eV) in  $\text{Ti}_3\text{SiC}_2$ , require the lowest energy among these intrinsic defect modes. Such antisite defects are therefore the most stable and most easily formed in these two typical 312-type MAX phases. Considering the formation of antisite defects, we [14,15] studied the microstructural evolution in  $\text{Ti}_3\text{AlC}_2$  and  $\text{Ti}_2\text{AlC}$  after irradiation and propose a mechanism for the observed irradiation-induced phase transitions. Due to the similarity of the structures and the bonding characteristic between  $\text{Ti}_2\text{AlC}$  and  $\text{Ti}_2\text{AlN}$ , the calculations performed here show that the antisite defect pair in  $\text{Ti}_2\text{AlN}$ ,  $\text{Al}_{\text{Ti}}\text{-Ti}_{\text{Al}}$ , exhibits the lowest formation energy (2.52 eV) among the various defects [25], as expected. Therefore, it is assumed that ion irradiation drives the uniform rearrangement of the cation atoms into a solid solution on the cation sublattice, which leads to a phase transformation to the  $\gamma$ - $\text{Ti}_2\text{AlN}$  phase. Energy-dispersive X-ray spectroscopy (EDS) was performed during the TEM analysis, and the results are shown in Table 3, to confirm that its stoichiometry was retained under irradiation and that the observed transformation depends only on disordering, rather than decomposition. The proposed structure of the  $\gamma$ - $\text{Ti}_2\text{AlN}$  phase, shown in Fig. 8(a), consists of an hcp-like structure wherein the Ti and Al atoms occupy a single cation site with a ratio of 2:1, as a solid solution. Based on the SAED pattern (Fig. 4(a)), the unit cell parameters of this structure are,  $a = 0.302 \text{ nm}$ ,  $c = 1.395 \text{ nm}$ , which means that the  $a$  parameter slightly shrinks and the  $c$  parameter expands as compared with the unit cell parameters obtained from the SAED pattern of the unirradiated sample ( $a = 0.306 \text{ nm}$ ,  $c = 1.360 \text{ nm}$ ). The accumulation of this anisotropic expansion of the unit cell causes cracking mostly along grain boundaries [40,41], which degrades the mechanical properties of the material. However, the corresponding simulated EDPs along  $[11\bar{2}0]$  and  $[1\bar{1}00]$ , shown in Fig. 8(a), are not in agreement with the experimental SAED patterns, indicating that the proposed structure is incorrect.

To further elucidate the structure of this phase, it is necessary to consider additional defect modes that might be induced by irradiation. Compared with the formation energy of Ti Frenkel pairs (7.21 eV) and Al Frenkel pairs (5.42 eV), the formation energy of N Frenkel pairs is relatively low (3.56 eV) [25], implying that N atoms may be readily displaced from their initial positions by nuclear collisions. Therefore, besides the formation of antisite defects mentioned above, additional processes in the formation of the  $\gamma$ - $\text{Ti}_2\text{AlN}$  phase are proposed: some of the N atoms, which were initially located at the octahedral sites between the Ti layers in the pristine sample, move to new interstitial octahedral sites between the rearranged cation layers, on which Ti and Al atoms are distributed uniformly. Meanwhile, due to the formation of antisite defects and the rearrangement of the N atoms, the interlayer

spacing gradually becomes homogeneous, yielding the observed attenuation of the  $(000l)$  ( $l \neq 3n$ ) diffraction spots according to the systematic principle of electron diffraction. This is consistent with the experimental results (insets in Fig. 8(b)). Hence, the structure of the  $\gamma$ - $\text{Ti}_2\text{AlN}$  phase entails both the formation of antisite defects and the rearrangement of the N atoms, as shown in Fig. 8 (b). The specific positions of Ti and Al atoms are indistinguishable at the cation sites, and the N atoms randomly occupy the octahedral sites with a vacancy ratio of 0.67. The EDPs simulated using this proposed structure show that the  $(000l)$  ( $l \neq 3n$ ) and the  $(\bar{1}10l)$  ( $l \neq 3n$ ) diffraction spots along  $[11\bar{2}0]$  as well as  $(000l)$  ( $l \neq 6n$ ) and  $(11\bar{2}l)$  ( $l \neq 6n$ ) diffraction spots along  $[1\bar{1}00]$  disappear, which is in agreement with the experimental SAED patterns (see Fig. 8(b) insets) obtained from the sample irradiated to  $3 \times 10^{14} \text{ cm}^{-2}$ . The only discrepancy is that the  $(0003)$  spot, indicated by a red dashed circle, can be observed in the SAED pattern along  $[11\bar{2}0]$ , which can be attributed to double diffraction generated by the vector addition of the  $(\bar{1}100)$  and the  $(1\bar{1}03)$  spots. In order to further confirm this proposed structure of the  $\gamma$ - $\text{Ti}_2\text{AlN}$  phase, phase contrast simulations along  $[11\bar{2}0]$  were performed. These simulations allow for comparison of the phase contrast and the stacking sequences corresponding to the proposed structure with the experimental results. The simulations were performed in various defocus and thickness permutations. The simulated image is superimposed onto the experimental HRTEM image in Fig. 8 (c), revealing a consistent relation.

In a previous study on the structural evolution of  $\text{Cr}_2\text{AlC}$  after irradiation [21], ion irradiation was shown to trigger a phase transformation to a  $\gamma$ - $\text{Cr}_2\text{AlC}$  phase, which has a structure similar to an intermediated hcp  $(\text{Cr},\text{Al})_2\text{C}_x$  phase (prototype  $\text{Fe}_2\text{N}$ ,  $P6_3/mmc$ ) that forms during the crystallization of  $\text{Cr}_2\text{AlC}$  from an amorphous phase [42]. The proposed structure of  $\gamma$ - $\text{Cr}_2\text{AlC}$ , which is based on the structure of  $(\text{Cr},\text{Al})_2\text{C}_x$ , is consistent with the experimental results. Therefore, considering the structural similarity of  $\text{Cr}_2\text{AlC}$  and  $\text{Ti}_2\text{AlN}$ , it is deduced that  $\text{Ti}_2\text{AlN}$  also undergoes a phase transformation to a  $\gamma$ - $\text{Ti}_2\text{AlN}$  phase, which has the same structure as hcp  $\text{TiN}_{0.3}$  [43]. However, the diffraction peak positions of the  $\gamma$ - $\text{Ti}_2\text{AlN}$  phase (see Fig. 3(a)) and the  $\text{TiN}_{0.3}$  phase have slight deviations, which results from the different Al occupancy and N vacancy ratio. Nonetheless, the simulated EDPs and the phase contrast of the proposed  $\gamma$ - $\text{Ti}_2\text{AlN}$  phase are consistent with the SAED patterns and the HRTEM images. These comparisons further confirm that, at low fluences, the transformation to  $\gamma$ - $\text{Ti}_2\text{AlN}$  is driven by the formation of antisite defects and the rearrangement of anion atoms.

At fluences above those at which the  $\gamma$ -phase forms, the XRD and TEM results show an obvious phase transformation to an fcc structure with twinned sequences of ABCABC and CBACBA along  $[111]$ , as shown in Fig. 9 (a). This twinned stacking structure results from the increasing number of extended defects (including dislocations and related stacking faults) induced by ion irradiation damage. Since the formation energy of a dislocation is proportional

**Table 3**

Chemical compositions (at. %) of virginal and irradiated  $\text{Ti}_2\text{AlX}$  ( $X = \text{C}, \text{N}$ ) and  $\text{Ti}_4\text{AlN}_3$  at different fluences.

	Fluence ( $\text{cm}^{-2}$ )	Ti	Al	N	C
$\text{Ti}_2\text{AlN}$	Virgin	$38.58 \pm 0.21$	$19.94 \pm 0.11$	$41.47 \pm 0.69$	/
	$1 \times 10^{15}$	$39.28 \pm 0.25$	$20.43 \pm 0.13$	$40.27 \pm 0.69$	/
	$2 \times 10^{16}$	$39.16 \pm 0.22$	$20.55 \pm 0.12$	$40.28 \pm 0.83$	/
$\text{Ti}_2\text{AlC}$	Virgin	$37.66 \pm 0.38$	$19.59 \pm 0.21$	/	$42.72 \pm 0.41$
	$1 \times 10^{15}$	$38.04 \pm 0.40$	$20.26 \pm 0.20$	/	$41.69 \pm 0.37$
	$2 \times 10^{16}$	$37.99 \pm 0.53$	$19.26 \pm 0.15$	/	$42.75 \pm 0.31$
$\text{Ti}_4\text{AlN}_3$	Virgin	$38.31 \pm 0.29$	$10.84 \pm 0.11$	$50.84 \pm 1.26$	/
	$1 \times 10^{15}$	$37.97 \pm 0.16$	$10.43 \pm 0.06$	$51.59 \pm 0.21$	/
	$2 \times 10^{16}$	$38.56 \pm 0.16$	$10.65 \pm 0.06$	$50.78 \pm 0.20$	/

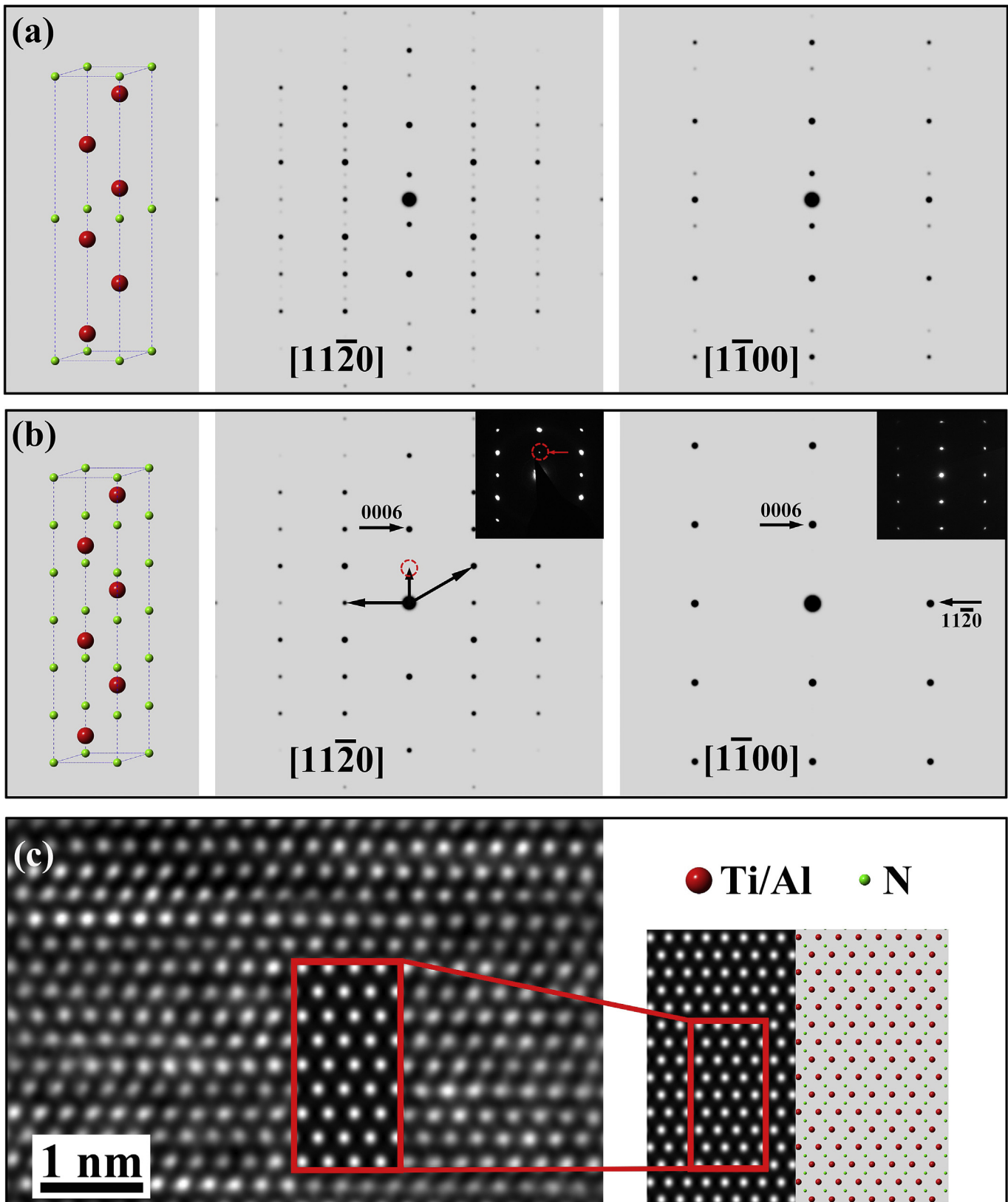


**Fig. 8.** The unit cells and the corresponding EDPs along  $[11\bar{2}0]$  and  $[1\bar{1}00]$  of the proposed  $\gamma$ -Ti<sub>2</sub>AlN structures at  $3 \times 10^{14} \text{ cm}^{-2}$  (a, b) as well as the simulated phase contrast image associated with the revised structure (c). The corresponding experimental SAED patterns are shown in the insets for convenient comparison. The weak diffraction spot marked by the red dotted circle represents the (0003) diffraction spot shown in the SAED pattern due to double diffraction indicated by the black vector arrow plot. (For interpretation of the references to colour in this figure legend, the reader is referred to the web version of this article.)

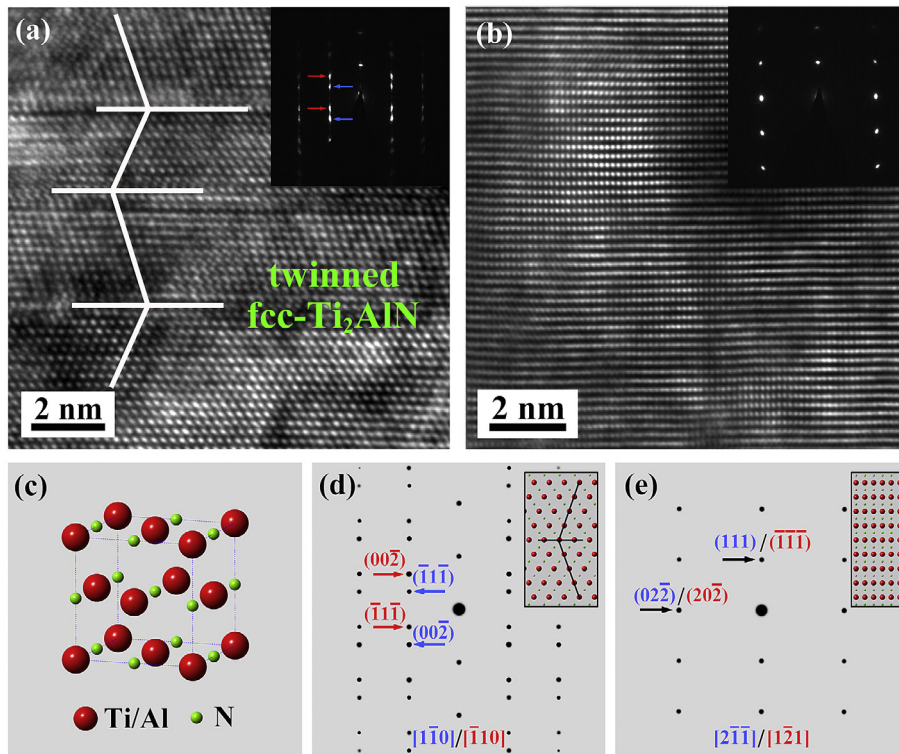


**Fig. 9.** HRTEM images along  $[1\bar{1}\bar{2}0]$  (a) and  $[1\bar{1}00]$  (b) of  $\text{Ti}_2\text{AlN}$  irradiated with  $1 \text{ MeV Au}^+$  ions to a fluence of  $1 \times 10^{16} \text{ cm}^{-2}$ , as well as the proposed fcc structure (c) and the simulated EDPs along  $[1\bar{1}0]/[\bar{1}10]$  (d) and  $[2\bar{1}1]/[1\bar{2}1]$  (e), which are consistent with the SAED patterns.

to the square of a material's Burgers vector,  $b^2$ ,  $\frac{1}{3}(11\bar{2}0)(0001)$  dislocations are the most energetically favored, such that almost all of these dislocations are located at the  $(0001)$  basal plane. Generally, for hcp MAX phases, the dissociation reactions of these perfect  $\frac{1}{3}(11\bar{2}0)(0001)$  dislocations occur in the basal plane and can be expressed as

$$\frac{1}{3}(11\bar{2}0) \rightarrow \frac{1}{3}(10\bar{1}0) + \text{Stacking Fault} + \frac{1}{3}(01\bar{1}0) \quad (1)$$

that generates stacking faults bounded by two partial dislocations [44]. The formation of stacking faults changes the local stacking sequences and results in the further phase transition to a rocksalt-like fcc structure ( $Fm\bar{3}m$ ) as shown in Fig. 9 (c). Fig. 9 (d and e) present the atomic arrangements of the  $(111)$  twinned fcc structure, as well as the simulated EDPs along  $[1\bar{1}0]/[\bar{1}10]$  and  $[2\bar{1}1]/[1\bar{2}1]$ , which is consistent with the experimental SAED patterns in Fig. 9(a and b) insets. The formation of an fcc structure from the hcp structure has also been observed in some C-based MAX phases [15,45]. It should be noted that both the  $\gamma$ - $\text{Ti}_2\text{AlN}$  phase and the fcc- $\text{Ti}_2\text{AlN}$  phase are solid solutions,  $(\text{Ti}_{0.67}\text{Al}_{0.33})\text{N}_{0.33}$ , in which Ti and Al atoms randomly occupy the cation sites and N atoms occupy the anion sites with the vacancy ratio of 0.67, respectively.

#### 4.2. Susceptibility to radiation-induced phase transitions of $\text{Ti}_2\text{AlX}$ ( $X = \text{C}, \text{N}$ ): the role of the $X$ factor

Since the response of materials to ion irradiation is closely related to the nature of their interatomic interactions [46], composition and bonding characteristics play an important role in their susceptibility to radiation-induced phase transitions. For example, in previous studies, Lian et al. [47] investigated the structural evolution of titanate and zirconate pyrochlores ( $\text{A}_2\text{B}_2\text{O}_7$ ,

$\text{A} = \text{Gd, Er, Lu, B} = \text{Ti, Zr}$ ) after irradiation. Based on the EDP simulations, they concluded that the formation of cation antisite defects, accompanied by disordering of the anion atoms with constitutional vacancies, yielded a phase transition from pyrochlore to a defect-fluorite structure. This process and the mechanism of the observed phase transition is similar to that of  $\text{Ti}_2\text{AlN}$  under  $\text{Au}^+$  ion irradiation. Clear composition dependencies of radiation-induced phase transitions have also been found in a variety of other ceramics, such as the titanate ( $\text{A}_2\text{Ti}_2\text{O}_7$  [47,48]) and stannate ( $\text{A}_2\text{Sn}_2\text{O}_7$  [49]) pyrochlores, as well as the lanthanide sesquioxides ( $\text{Ln}_2\text{O}_3$  [50]).

The XRD and TEM results show that the susceptibilities of  $\text{Ti}_2\text{AlN}$  and  $\text{Ti}_2\text{AlC}$  to the radiation-induced phase transition from hcp to fcc structures are comparable. At the first step of the phase transformation,  $\gamma$ - $\text{Ti}_2\text{AlN}$  and  $\gamma$ - $\text{Ti}_2\text{AlC}$  ( $a = 0.303 \text{ nm}$ ,  $c = 1.393 \text{ nm}$ ) phases were observed, though their stacking sequences differ. This might be attributed to the fact that there exists no hcp-structure phase of  $\text{Ti}_2\text{X}$  (and thus no hcp-(Ti,Al)C solid solution), while there does exist an hcp phase of  $\text{Ti}_2\text{N}$  [43]. At higher fluences, from  $1 \times 10^{15}$  to  $2 \times 10^{16} \text{ cm}^{-2}$ , the fcc- $\text{Ti}_2\text{AlX}$  ( $X = \text{C}, \text{N}$ ) phases gradually form, and the processes of these transitions are similar. The peaks from both the transformed fcc structure and the initial hcp structure broaden pronouncedly with increasing fluence, due to large number of irradiation-induced defects, such that it is difficult to perform Rietveld refinement to obtain the quantitative ratio of the fcc phase to the hcp phase. However, at a fluence of  $1 \times 10^{16} \text{ cm}^{-2}$ , the  $(101)$  peak of the  $\gamma$ - $\text{Ti}_2\text{AlN}$  phase almost disappears, while it still remains in  $\text{Ti}_2\text{AlC}$ . This is verified by the corresponding TEM results, shown in Figs. 4 and 5. This indicates that  $\text{Ti}_2\text{AlC}$  is slightly more resistant to the radiation-induced phase transitions, though the difference is minor. In addition,  $\text{TiC}$  and  $\text{TiN}$  are known for their extreme stabilities under irradiation [51,52], which can be explained by their efficient dissipation of the energy deposited

along the particle paths as non-damaging thermal energy. Therefore, in the irradiation of these MAX phases, there occurs no amorphization because the  $\text{Ti}_2\text{C}$  and  $\text{Ti}_2\text{N}$  slabs interleaved by Al layers, as the main parts of  $\text{Ti}_2\text{AlC}$  and  $\text{Ti}_2\text{AlN}$ , play an important role in the radiation tolerance.

Fig. 10 shows the calculated total electron density of states (TDOS) of  $\text{Ti}_2\text{AlN}$  and  $\text{Ti}_2\text{AlC}$ , as well as their atomic and orbital projected DOS. There is a non-zero TDOS value at the Fermi level ( $E_F$ ) in both  $\text{Ti}_2\text{AlN}$  and  $\text{Ti}_2\text{AlC}$ , consistent with their metallic properties. For  $\text{Ti}_2\text{AlC}$ , the TDOS around  $E_F$  is at a local minimum in contrast to that of  $\text{Ti}_2\text{AlN}$ , indicating that  $\text{Ti}_2\text{AlC}$  is more stable than  $\text{Ti}_2\text{AlN}$ . In addition, the DOS hybridization of Ti-Al in  $\text{Ti}_2\text{AlC}$  is located at around  $-1$  eV, while that of Ti-Al in  $\text{Ti}_2\text{AlN}$  is around  $-2$  eV. The closer location to  $E_F$  indicates that Ti-Al in  $\text{Ti}_2\text{AlC}$  exhibits weaker bond covalency than Ti-Al in  $\text{Ti}_2\text{AlN}$ . Thus, the weaker bonding of Ti-Al in  $\text{Ti}_2\text{AlC}$  is more ionic. Trachenko et al. have shown that the long-range forces associated with ionic bonding promote the recovery of material that has been damaged by irradiation to its initial crystalline state, relative to covalent bonding [46,53]. Therefore, the ionic character of the cation-cation

bonds in  $\text{Ti}_2\text{AlC}$  facilitates the recovery of damaged regions to a crystalline structure and requires less energy for the reconstruction of the bond after it has been broken by atomic displacement. This possibly explains the slightly superior radiation tolerance of  $\text{Ti}_2\text{AlC}$  relative to  $\text{Ti}_2\text{AlN}$ , as the irradiation-induced phase transformations specifically entail the disordering of the cation sublattices.

Another important observation is the high degree of hybridization of  $\text{Ti}(3d)$  orbitals and  $\text{X}(2p)$  orbitals observed in the DOS, revealing a strong covalent interaction between Ti-X in these two MAX phases. The DOS simulation results show that the hybridization of  $\text{Ti}3d\text{-C}2s$  and  $\text{Ti}3d\text{-C}2p$  in  $\text{Ti}_2\text{AlC}$  are located at lower energy than the hybridization of  $\text{Ti}3d\text{-N}2s$  and  $\text{Ti}3d\text{-N}2p$  in  $\text{Ti}_2\text{AlN}$ . These simulation results lead to the conclusion that the Ti-C bond is less covalent than the Ti-N bond, enhancing the stability of  $\text{Ti}_2\text{AlC}$  when the system is disturbed by irradiation, relative to the nitride. However, the differences between  $\text{Ti}_2\text{AlC}$  and  $\text{Ti}_2\text{AlN}$  are subtle, which is consistent with the experimental results showing only a small difference in radiation tolerance. This result is in good agreement with those obtained from neutron irradiation [54], which also indicated that, at a given neutron fluence,  $\text{Ti}_2\text{AlC}$

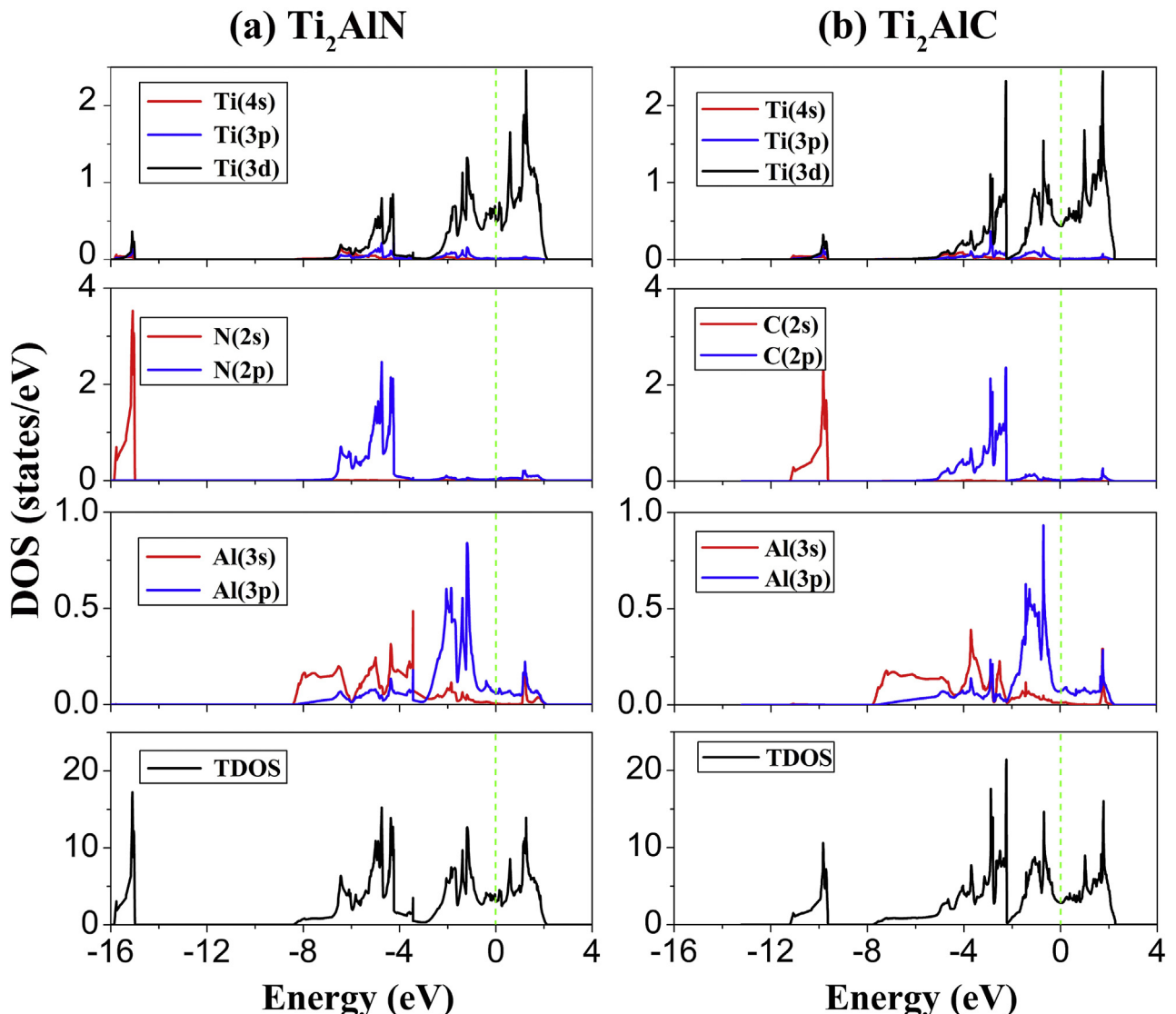


**Fig. 10.** Calculated density of states and partial density of states for (a)  $\text{Ti}_2\text{AlN}$  and (b)  $\text{Ti}_2\text{AlC}$ . The green line is plotted to indicate DOS at Fermi level. (For interpretation of the references to colour in this figure legend, the reader is referred to the web version of this article.)

retained a greater fraction of its hcp structure than Ti<sub>2</sub>AlN.

#### 4.3. Susceptibility to radiation-induced phase transitions of Ti<sub>2</sub>AlN and Ti<sub>4</sub>AlN<sub>3</sub>: the role of the *n* factor

The XRD results show that Au<sup>+</sup> ion irradiation also triggers phase transformation from the hcp to the fcc structure in Ti<sub>4</sub>AlN<sub>3</sub>, which is confirmed by the TEM results [55]. At a fluence of  $1 \times 10^{15} \text{ cm}^{-2}$ , the phase transformation of Ti<sub>2</sub>AlN to the fcc structure is evident. In contrast, the hcp structure of Ti<sub>4</sub>AlN<sub>3</sub> remains dominant at this fluence, despite extensive distortion of the structure and transformation to the hcp structured  $\gamma$ -Ti<sub>4</sub>AlN<sub>3</sub>. In addition, Ti<sub>2</sub>AlN is completely transformed to the fcc structure at  $2 \times 10^{16} \text{ cm}^{-2}$ , while there remains a considerable amount of the hcp phase in Ti<sub>4</sub>AlN<sub>3</sub>. These comparisons clearly yield the conclusion that Ti<sub>4</sub>AlN<sub>3</sub> is much more resistant to irradiation-induced phase transition than in Ti<sub>2</sub>AlN.

With the same chemical elements, the only structural difference between these two pristine materials is the number of Ti (edge-sharing Ti<sub>6</sub>N octahedra) layers interleaved between close-packed Al layers, i.e., 4 layers in Ti<sub>4</sub>AlN<sub>3</sub> and 2 layers in Ti<sub>2</sub>AlN, as shown in Fig. 2. As discussed in Section 4.2, the covalent Ti-N bond is stronger than the Ti-Al bonds, and the strength of these Ti-N bonds hinders the migration of Ti atoms [56]. Meanwhile, the Al atoms are more readily displaced from their initial positions by nuclear collisions. It is evident that the number of Ti-N bonds in Ti<sub>4</sub>AlN<sub>3</sub> is higher, and the number of Al layers is lower than that in Ti<sub>2</sub>AlN, which makes Ti<sub>4</sub>AlN<sub>3</sub> more stable under irradiation. A similar compositional trend has been observed in the C-based MAX phases [57].

In the ion-irradiation-induced phase transition systematics in Ti<sub>2</sub>AlN, both  $\gamma$ -Ti<sub>2</sub>AlN and the fcc-Ti<sub>2</sub>AlN are considered solid solutions, i.e.,  $\gamma$ -(Ti<sub>0.67</sub>Al<sub>0.33</sub>)N<sub>0.33</sub> and fcc-(Ti<sub>0.67</sub>Al<sub>0.33</sub>)N<sub>0.33</sub>, in which Ti and Al atoms uniformly occupy the cation sites with an occupancy ratio of 2:1 and N atoms occupy the anion sites with the vacancy ratio of 0.67. Likewise, the  $\gamma$ -Ti<sub>4</sub>AlN<sub>3</sub> phase and the fcc-Ti<sub>4</sub>AlN<sub>3</sub> phase induced by ion irradiation are also regarded as solid solutions, i.e.,  $\gamma$ -(Ti<sub>0.8</sub>Al<sub>0.2</sub>)N<sub>0.6</sub> and fcc-(Ti<sub>0.8</sub>Al<sub>0.2</sub>)N<sub>0.6</sub>. There are two main structural differences between the (Ti<sub>0.67</sub>Al<sub>0.33</sub>)N<sub>0.33</sub> and (Ti<sub>0.8</sub>Al<sub>0.2</sub>)N<sub>0.6</sub> solid solutions, with the assumption that no Al or N atoms escape from the sample after irradiation: (1) the Al occupancy of the cation sites depends on the number of Ti layers interleaved by close-packed Al layers, thus, the Al site occupancy in (Ti<sub>0.8</sub>Al<sub>0.2</sub>)N<sub>0.6</sub> is 0.2, which is lower than that in (Ti<sub>0.67</sub>Al<sub>0.33</sub>)N<sub>0.33</sub>, 0.33; (2) the N vacancy ratio in the anion sites is 0.67 in (Ti<sub>0.67</sub>Al<sub>0.33</sub>)N<sub>0.33</sub> and 0.4 in (Ti<sub>0.8</sub>Al<sub>0.2</sub>)N<sub>0.6</sub>.

In the XRD patterns (see Fig. 3), the position of the (200) peak of fcc-Ti<sub>4</sub>AlN<sub>3</sub> is different from that from the TiN impurity with the same fcc structure, which demonstrates that the occupancy of Al atoms in the cation sites and the N vacancy in the anion sites leads

to a variation in the unit cell parameter. The (002) peaks of the fcc-(Ti<sub>0.67</sub>Al<sub>0.33</sub>)N<sub>0.33</sub>, fcc-(Ti<sub>0.8</sub>Al<sub>0.2</sub>)N<sub>0.6</sub> solid solutions, and the binary fcc-TiN impurities are located at  $2\theta = 44.25^\circ$ ,  $43.60^\circ$ , and  $42.80^\circ$ , respectively. According to Bragg's Law, the corresponding *a* unit cell parameters are 0.411 nm, 0.417 nm, and 0.424 nm, respectively, as displayed in Table 4, indicating that the volume of the fcc unit cell decreases with the increase of Al occupancy and N vacancy concentrations. This result is confirmed by the HRTEM measurements in Fig. 5 (c and i), though the deviation is minor. This compositional trend may arise from the fact that the higher Al occupancy in (Ti<sub>0.67</sub>Al<sub>0.33</sub>)N<sub>0.33</sub> leads to more severe structural distortion, which is consistent with the trend of the distortion in binary TiN doped with varying concentrations of Al [58]. Meanwhile, in the transformed metastable (Ti<sub>0.67</sub>Al<sub>0.33</sub>)N<sub>0.33</sub> and (Ti<sub>0.8</sub>Al<sub>0.2</sub>)N<sub>0.6</sub> solid solutions, the higher N anion vacancy ratio in (Ti<sub>0.67</sub>Al<sub>0.33</sub>)N<sub>0.33</sub> decreases the stability of the system and facilitates the order-to-disorder transition [59].

Using the same method of analysis, the *a* unit cell parameters of fcc-(Ti<sub>0.67</sub>Al<sub>0.33</sub>)C<sub>0.33</sub> (Ti<sub>2</sub>AlC after irradiation, see Fig. 3), fcc-(Ti<sub>0.75</sub>Al<sub>0.25</sub>)C<sub>0.5</sub> (Ti<sub>3</sub>AlC<sub>2</sub> after irradiation) solid solutions, and the binary fcc-TiC are 0.421 nm, 0.425 nm, and 0.433 nm, respectively, shown in Table 5. Comparison of the unit cell parameters for all of these C-based compounds is consistent with that from the N-based MAX phases discussed above. Therefore, it is deduced that M<sub>n+1</sub>AX<sub>n</sub> phases with larger *n*, but composed of the same constituent elements exhibit better stability and higher resistance to irradiation-induced structural phase transitions due to their lower Al content and lower anion vacancy ratio in the irradiation-induced fcc phases.

## 5. Conclusions

The irradiation-induced phase transitions in Ti<sub>2</sub>AlN, Ti<sub>2</sub>AlC and Ti<sub>4</sub>AlN<sub>3</sub> have been investigated by GIXRD, TEM, and first-principles calculations. The formation of intermediate  $\gamma$ -phases and final fcc phases were observed, and their associated structures have been determined, using EDP and phase contrast simulation. The formation of intermediate  $\gamma$ -phases from the initial hcp phases is driven by the production of cation antisite defects and a corresponding rearrangement of anions. The occurrence of extended defects, including stacking faults, contributes to the transition from the  $\gamma$ -phases to the fcc phases. These transformed phases are considered as solid solutions wherein the cations occupy a single site and the anions are randomly arranged on a partially occupied sublattice.

By comparing the radiation responses of Ti<sub>2</sub>AlN, Ti<sub>2</sub>AlC and Ti<sub>4</sub>AlN<sub>3</sub>, the role of X and *n* factors in the radiation tolerance of M<sub>n+1</sub>AX<sub>n</sub> was investigated. Similar phase transitions from hcp to fcc structures were found in all three compounds, yet the threshold fluences for the transitions differ. For Ti<sub>2</sub>AlX (X = C, N), Ti<sub>2</sub>AlC is slightly less susceptible to the radiation-induced phase transformation than Ti<sub>2</sub>AlN. This is attributed to the stronger Ti-Al bond covalency in Ti<sub>2</sub>AlN than that of the Ti-Al bonds in Ti<sub>2</sub>AlC, which could result in a higher efficiency of damage recovery in Ti<sub>2</sub>AlC. The MAX phases with higher *n* values are more resistant to radiation-induced phase transitions than those MAX phases with lower *n* values, but composed of the same constituent elements, (i.e., the

**Table 4**

Unit cell parameters of the fcc structural Ti<sub>2</sub>AlN, Ti<sub>4</sub>AlN<sub>3</sub> and TiN.

unit cell parameter ( <i>a</i> )	fcc-(Ti <sub>0.67</sub> Al <sub>0.33</sub> )N <sub>0.33</sub>	fcc-(Ti <sub>0.8</sub> Al <sub>0.2</sub> )N <sub>0.6</sub>	fcc-TiN
XRD	0.411 nm	0.417 nm	0.424 nm
TEM	0.413 nm	0.418 nm	—

**Table 5**

Unit cell parameters of the fcc structural Ti<sub>2</sub>AlC, Ti<sub>3</sub>AlC<sub>2</sub> and TiC.

unit cell parameter ( <i>a</i> )	fcc-(Ti <sub>0.67</sub> Al <sub>0.33</sub> )C <sub>0.33</sub>	fcc-(Ti <sub>0.75</sub> Al <sub>0.25</sub> )C <sub>0.5</sub> <sup>a</sup>	fcc-TiC [63]
XRD	0.421 nm	0.425 nm	0.433 nm
TEM	0.421 nm	0.423 nm	—

<sup>a</sup> The XRD pattern and the TEM images of Ti<sub>3</sub>AlC<sub>2</sub> after irradiation are not shown in this paper.

tolerance of  $Ti_4AlN_3$  is superior to that of  $Ti_2AlN$ ; the tolerance of  $Ti_3AlC_2$  is superior to that of  $Ti_2AlC$ . This trend is caused by the different stabilities of the irradiation-induced solid solution phases due to the differing Al contents and anion vacancy ratios in the irradiation-induced phases. Although this study provides promising results for understanding the mechanisms of irradiation-induced phase transitions, for the use of MAX phases in the nuclear applications, further work is needed to clarify the nature of such phase transformation processes under reactor-specific conditions.

## Acknowledgments

This work was financially supported by the National Magnetic Confinement Fusion Energy Research Project of China (2015GB113000) and the National Natural Science Foundation of China (11675005). CLT and RCE contributed to the analysis of the data and were supported by the Energy Frontier Research Center “Materials Science of Actinides” funded by the U.S. Department of Energy (DOE), Office of Science, Office of Basic Energy Sciences (Grant No. DE-SC0001089). Part of this work was performed at the Stanford Nano Shared Facilities (SNSF), supported by the National Science Foundation under award ECCS-1542152. The authors thank the staff of Beijing Synchrotron Radiation Facility (BSRF) for the GIXRD measurements.

## References

- [1] Z.M. Sun, Progress in research and development on MAX phases: a family of layered ternary compounds, *Int. Mater. Rev.* 56 (3) (2011) 143–166.
- [2] M. Barsoum, H.-I. Yoo, I. Polushina, V.Y. Rud, Y.V. Rud, T. El-Raghy, Electrical conductivity, thermopower, and Hall effect of  $Ti_3AlC_2$ ,  $Ti_4AlN_3$ , and  $Ti_3SiC_2$ , *Phys. Rev. B* 62 (15) (2000) 10194.
- [3] D. Li, Y. Liang, X. Liu, Y. Zhou, Corrosion behavior of  $Ti_3AlC_2$  in NaOH and  $H_2SO_4$ , *J. Eur. Ceram. Soc.* 30 (15) (2010) 3227–3234.
- [4] M. Radovic, M.W. Barsoum, MAX phases: bridging the gap between metals and ceramics, *Am. Ceram. Soc. Bull.* 92 (3) (2013) 20–27.
- [5] H.B. Zhang, Y.C. Zhou, Y.W. Bao, M.S. Li, Abnormal thermal shock behavior of  $Ti_3SiC_2$  and  $Ti_3AlC_2$ , *J. Mater. Res.* 21 (09) (2011) 2401–2407.
- [6] P. Eklund, M. Beckers, U. Jansson, H. Höglberg, L. Hultman, The  $M_{n+1}AX_n$  phases: materials science and thin-film processing, *Thin Solid Films* 518 (8) (2010) 1851–1878.
- [7] J. Wang, Y. Zhou, Recent progress in theoretical prediction, preparation, and characterization of layered ternary transition-metal carbides, *Annu. Rev. Mater. Res.* 39 (1) (2009) 415–443.
- [8] Z.J. Lin, M.S. Li, Y.J. Wang, Y.C. Zhou, High-temperature oxidation and hot corrosion of  $Ti_2AlC$ , *Acta Mater.* 55 (18) (2007) 6182–6191.
- [9] E. Hoffman, D. Vinson, R. Sindelar, D. Tallman, G. Kohse, M. Barsoum, MAX phase carbides and nitrides: properties for future nuclear power plant in-core applications and neutron transmutation analysis, *Nucl. Eng. Des.* 244 (2012) 17–24.
- [10] T.R. Allen, R.J.M. Konings, A.T. Motta, 5.03-Corrosion of zirconium alloys, in: R.J.M. Konings (Ed.), *Comprehensive Nuclear Materials*, Elsevier, Oxford, 2012, pp. 49–68.
- [11] C. Wang, T. Yang, S. Kong, J. Xiao, J. Xue, Q. Wang, C. Hu, Q. Huang, Y. Wang, Effects of He irradiation on  $Ti_3AlC_2$ : damage evolution and behavior of He bubbles, *J. Nucl. Mater.* 440 (1–3) (2013) 606–611.
- [12] M.K. Patel, D.J. Tallman, J.A. Valdez, J. Aguiar, O. Anderoglu, M. Tang, J. Griggs, E. Fu, Y. Wang, M.W. Barsoum, Effect of helium irradiation on  $Ti_3AlC_2$  at 500 °C, *Scr. Mater.* 77 (2014) 1–4.
- [13] X. Liu, M. Le Flem, J.-L. Béchade, F. Onimus, T. Cozzika, I. Monnet, XRD investigation of ion irradiated  $Ti_3Si_{0.90}Al_{0.10}C_2$ , *Nucl. Instrum. Methods Phys. Res. Sect. B Beam Interact. Mater. Atoms* 268 (5) (2010) 506–512.
- [14] T. Yang, C. Wang, C.A. Taylor, X. Huang, Q. Huang, F. Li, L. Shen, X. Zhou, J. Xue, S. Yan, Y. Wang, The structural transitions of  $Ti_3AlC_2$  induced by ion irradiation, *Acta Mater.* 65 (2014) 351–359.
- [15] C. Wang, T. Yang, J. Xiao, S. Liu, J. Xue, J. Wang, Q. Huang, Y. Wang, Irradiation-induced structural transitions in  $Ti_2AlC$ , *Acta Mater.* 98 (2015) 197–205.
- [16] M. Bugnet, V. Mauchamp, P. Eklund, M. Jaouen, T. Cabioch, Contribution of core-loss fine structures to the characterization of ion irradiation damages in the nanolaminated ceramic  $Ti_3AlC_2$ , *Acta Mater.* 61 (19) (2013) 7348–7363.
- [17] M. Radovic, M. Barsoum, A. Ganguly, T. Zhen, P. Finkel, S. Kalidindi, E. Lara-Curcio, On the elastic properties and mechanical damping of  $Ti_3SiC_2$ ,  $Ti_3GeC_2$ ,  $Ti_3Si_{0.5}Al_{0.5}C_2$  and  $Ti_2AlC$  in the 300–1573 K temperature range, *Acta Mater.* 54 (10) (2006) 2757–2767.
- [18] W. Yu, V. Mauchamp, T. Cabioch, D. Magne, L. Gence, L. Piraux, V. Gauthier, Brunet, S. Dubois, Solid solution effects in the  $Ti_2Al(C_xN_y)$  MAX phases: synthesis, microstructure, electronic structure and transport properties, *Acta Mater.* 80 (2014) 421–434.
- [19] Y. Mo, P. Rulis, W.Y. Ching, Electronic structure and optical conductivities of 20 MAX-phase compounds, *Phys. Rev. B* 86 (16) (2012).
- [20] M. Baben, L. Shang, J. Emmerlich, J.M. Schneider, Oxygen incorporation in  $M_2Al$  ( $M = Ti, V, Cr$ ), *Acta Mater.* 60 (12) (2012) 4810–4818.
- [21] C. Wang, T. Yang, J. Xiao, S. Liu, J. Xue, Q. Huang, J. Zhang, J. Wang, Y. Wang, R. Koc, Structural transitions induced by ion irradiation in  $V_2AlC$  and  $Cr_2AlC$ , *J. Am. Ceram. Soc.* 99 (5) (2016) 1769–1777.
- [22] K.R. Whittle, M.G. Blackford, R.D. Augherson, S. Moricca, G.R. Lumpkin, D.P. Riley, N.J. Zaluzec, Radiation tolerance of  $M_{n+1}AX_n$  phases,  $Ti_3AlC_2$  and  $Ti_3SiC_2$ , *Acta Mater.* 58 (13) (2010) 4362–4368.
- [23] M. Bugnet, V. Mauchamp, E. Oliviero, M. Jaouen, T. Cabioch, Chemically sensitive amorphization process in the nanolaminated  $Cr_2AC$  ( $A = Al$  or  $Ge$ ) system from TEM in situ irradiation, *J. Nucl. Mater.* 441 (1–3) (2013) 133–137.
- [24] S. Zhao, J. Xue, Y. Wang, Q. Huang, Ab initio study of irradiation tolerance for different  $M_{n+1}AX_n$  phases:  $Ti_3SiC_2$  and  $Ti_3AlC_2$ , *J. Appl. Phys.* 115 (2) (2014) 023503.
- [25] J. Xiao, T. Yang, C. Wang, J. Xue, Y. Wang, Investigations on radiation tolerance of  $M_{n+1}AX_n$  Phases: study of  $Ti_3SiC_2$ ,  $Ti_2AlC$ ,  $Cr_2AlC$ ,  $Cr_2GeC$ ,  $Ti_2AlC$ , and  $Ti_2AlN$ , *J. Am. Ceram. Soc.* 98 (4) (2015) 1323–1331.
- [26] M.W. Barsoum, T. El-Raghy, A. Procopio, Synthesis of  $Ti_4AlN_3$  and phase equilibria in the Ti-Al-N system, *Metallurgical Mater. Trans. A* 31 (2) (2000) 373–378.
- [27] M. Yan, Y.-l. Chen, B.-c. Mei, J.-q. Zhu, Synthesis of high-purity  $Ti_2AlN$  ceramic by hot pressing, *Trans. Nonferrous Metals Soc. China* 18 (1) (2008) 82–85.
- [28] Z.J. Lin, M.J. Zhuo, Y.C. Zhou, M.S. Li, J.Y. Wang, Microstructural characterization of layered ternary  $Ti_2AlC$ , *Acta Mater.* 54 (4) (2006) 1009–1015.
- [29] J.F. Ziegler, M.D. Ziegler, J.P. Biersack, SRIM – the stopping and range of ions in matter (2010), *Nucl. Instrum. Methods Phys. Res. Sect. B Beam Interact. Mater. Atoms* 268 (11–12) (2010) 1818–1823.
- [30] C.O. Roar K. D. Bin, T. Kenji, S. Wharton, M. Laurence, EDM: Electron Direct Methods. <http://www.numis.northwestern.edu/edm/2006>.
- [31] G. Kresse, D. Joubert, From ultrasoft pseudopotentials to the projector augmented-wave method, *Phys. Rev. B* 59 (3) (1999) 1758.
- [32] P. Hohenberg, W. Kohn, Inhomogeneous electron gas, *Phys. Rev.* 136 (3B) (1964) B864–B871.
- [33] J.P. Perdew, J.A. Chevary, S.H. Vosko, K.A. Jackson, M.R. Pederson, D.J. Singh, C. Fiolhais, Atoms, molecules, solids, and surfaces: applications of the generalized gradient approximation for exchange and correlation, *Phys. Rev. B* 46 (11) (1992) 6671–6687.
- [34] P.E. Blöchl, Projector augmented-wave method, *Phys. Rev. B* 50 (24) (1994) 17953–17979.
- [35] H.J. Monkhorst, J.D. Pack, Special points for Brillouin-zone integrations, *Phys. Rev. B* 13 (12) (1976) 5188–5192.
- [36] G. Henkelman, B.P. Uberuaga, H. Jónsson, A climbing image nudged elastic band method for finding saddle points and minimum energy paths, *J. Chem. Phys.* 113 (22) (2000) 9901.
- [37] M.W. Barsoum, L. Farber, I. Levin, A. Procopio, T. El-Raghy, A. Berner, High-resolution transmission electron microscopy of  $Ti_4AlN_3$ , or  $Ti_3Al_2N_2$  revisited, *J. Am. Ceram. Soc.* 82 (9) (1999) 2545–2547.
- [38] Q. Qi, G.J. Cheng, L.Q. Shi, D.J. O’Connor, B.V. King, E.H. Kisi, Damage accumulation and recovery in  $C^+$ -irradiated  $Ti_3SiC_2$ , *Acta Mater.* 66 (2014) 317–325.
- [39] S.C. Middleburgh, G.R. Lumpkin, D. Riley, Y. Zhon, Accommodation, accumulation, and migration of defects in  $Ti_3SiC_2$  and  $Ti_3AlC_2$  MAX phases, *J. Am. Ceram. Soc.* 96 (10) (2013) 3196–3201.
- [40] D.W. Clark, S.J. Zinkle, M.K. Patel, C.M. Parish, High temperature ion irradiation effects in MAX phase ceramics, *Acta Mater.* 105 (2016) 130–146.
- [41] S. Liu, C. Wang, T. Yang, Y. Fang, Q. Huang, Y. Wang, High temperature effects on irradiation damage of  $Ti_2AlC$ , *Nucl. Instrum. Methods Phys. Res. Sect. B Beam Interact. Mater. Atoms* 406 (Part B) (2017) 662–669.
- [42] A. Abdulkadhim, M. to Baben, T. Takahashi, V. Schnabel, M. Hans, C. Polzer, P. Polcik, J.M. Schneider, Crystallization kinetics of amorphous  $Cr_2AlC$  thin films, *Surf. Coatings Technol.* 206 (4) (2011) 599–603.
- [43] W. Lengauer, P. Ettmayer, Investigations of phase equilibria in the Ti-N and Ti-Mo-N systems, *Mater. Sci. Eng. A* 105 (1988) 257–263.
- [44] R. Yu, Q. Zhan, L.L. He, Y.C. Zhou, H.Q. Ye, Stacking faults and grain boundaries of  $Ti_3SiC_2$ , *Philos. Mag. Lett.* 83 (5) (2003) 325–331.
- [45] T. Yang, C. Wang, W. Liu, S. Liu, J. Xiao, Q. Huang, J. Xue, S. Yan, Y. Wang, Formation of nano-twinned structure in  $Ti_3AlC_2$  induced by ion-irradiation, *Acta Mater.* 128 (2017) 1–11.
- [46] K. Trachenko, Understanding resistance to amorphization by radiation damage, *J. Phys. Condens. Matter* 16 (49) (2004) R1491.
- [47] J. Lian, L. Wang, J. Chen, K. Sun, R.C. Ewing, J. Matt Farmer, L.A. Boatner, The order-disorder transition in ion-irradiated pyrochlore, *Acta Mater.* 51 (5) (2003) 1493–1502.
- [48] J. Shamblin, C.L. Tracy, R.C. Ewing, F. Zhang, W. Li, C. Trautmann, M. Lang, Structural response of titanate pyrochlores to swift heavy ion irradiation, *Acta Mater.* 117 (2016) 207–215.
- [49] C.L. Tracy, J. Shamblin, S. Park, F. Zhang, C. Trautmann, M. Lang, R.C. Ewing, Role of composition, bond covalency, and short-range order in the disordering of stannate pyrochlores by swift heavy ion irradiation, *Phys. Rev. B* 94 (6)

- (2016) 064102.
- [50] C.L. Tracy, M. Lang, F. Zhang, C. Trautmann, R.C. Ewing, Phase transformations in  $\text{Ln}_2\text{O}_3$  materials irradiated with swift heavy ions, *Phys. Rev. B* 92 (17) (2015) 174101.
- [51] K. Hojou, H. Otsu, S. Furuno, K. Izui, T. Tsukamoto, In-situ observation of damage evolution in TiC crystals during helium ion irradiation, *J. Nucl. Mater.* 212 (1994) 281–286.
- [52] L. David, S. Gomes, G. Carlot, J. Roger, D. Fournier, C. Valot, M. Raynaud, Characterization of thermal conductivity degradation induced by heavy ion irradiation in ceramic materials, *J. Phys. D Appl. Phys.* 41 (3) (2008) 035502.
- [53] K. Trachenko, J. Pruneda, E. Artacho, M.T. Dove, How the nature of the chemical bond governs resistance to amorphization by radiation damage, *Phys. Rev. B* 71 (18) (2005) 184104.
- [54] D.J. Tallman, E.N. Hoffman, E.a.N. Caspi, B.L. Garcia-Diaz, G. Kohse, R.L. Sindelar, M.W. Barsoum, Effect of neutron irradiation on select MAX phases, *Acta Mater.* 85 (2015) 132–143.
- [55] C. Wang, T. Yang, C.-H. Chen, S. Park, S. Liu, Y. Fang, Z. Yan, J. Xue, J. Zhang, J. Wang, R.C. Ewing, Y. Wang, Ion-irradiation-induced structural evolution in  $\text{Ti}_4\text{AlN}_3$ , *Scr. Mater.* 133 (2017) 19–23.
- [56] Y. Zhou, Z. Sun, Electronic structure and bonding properties of layered machinable  $\text{Ti}_2\text{AlC}$  and  $\text{Ti}_2\text{AlN}$  ceramics, *Phys. Rev. B* 61 (19) (2000) 12570.
- [57] X. Wang, Y. Zhou, Layered machinable and electrically conductive  $\text{Ti}_2\text{AlC}$  and  $\text{Ti}_3\text{AlC}_2$  ceramics: a review, *J. Mater. Sci. Technol.* 26 (5) (2010) 385–416.
- [58] O. Knotek, M. Böhmer, T. Leyendecker, On structure and properties of sputtered Ti and Al based hard compound films, *J. Vac. Sci. Technol. A Vac. Surfaces. Films* 4 (6) (1986) 2695–2700.
- [59] V. Lipatnikov, A. Gusev, Dependence of the resistivity of nonstoichiometric titanium carbide  $\text{TiC}_y$  on the density and distribution of carbon vacancies, *J. Exp. Theor. Phys. Lett.* 70 (4) (1999) 294–300.
- [60] W.B. Zhou, B.C. Mei, J.Q. Zhu, X.L. Hong, Rapid synthesis of  $\text{Ti}_2\text{AlC}$  by spark plasma sintering technique, *Mater. Lett.* 59 (1) (2005) 131–134.
- [61] Z.J. Lin, M.J. Zhuo, M.S. Li, J.Y. Wang, Y.C. Zhou, Synthesis and microstructure of layered-ternary  $\text{Ti}_2\text{AlN}$  ceramic, *Scr. Mater.* 56 (12) (2007) 1115–1118.
- [62] C. Rawn, M. Barsoum, T. El-Raghy, A. Procipio, C. Hoffmann, C. Hubbard, Structure of  $\text{Ti}_2\text{AlN}_3$ —a layered  $\text{M}_{n+1}\text{AX}_n$  nitride, *Mater. Res. Bull.* 35 (11) (2000) 1785–1796.
- [63] C.-C. Jiang, T. Goto, T. Hirai, Non-stoichiometry of titanium nitride plates prepared by chemical vapour deposition, *J. Alloys Compd.* 190 (2) (1993) 197–200.